COMPUTATIONAL MODELING OF INDENTATION OF MATERIALS

BY

VINEET AGARWAL

THESIS

Submitted in partial fulfillment of the requirements
for the degree of Master of Science in Mechanical Engineering
in the Graduate College of the
University of Illinois at Urbana-Champaign, 2015

Urbana, Illinois

Adviser:

Professor Iwona Jasiuk

ABSTRACT

This thesis focusses on computational modeling of several different indentation problems involving the microindentation, nanoindentation and reference point indentation (RPI). The goal of this thesis is to develop better understanding of indentation processes in different materials utilizing numerical methods.

Indentation has been used for a long time for characterizing hardness of materials. Nanoindentation [1] is a technique where a micron scale indenter is forced into a material of interest while monitoring load and displacement. Indentation techniques can be used to measure elastic modulus, hardness and viscoelastic properties of materials [2]. The RPI technique [3] uses a reference probe which sits on the surface of substrate and defines datum for test probe. The test probe indents the substrate multiple times using a cyclic load and computes nine different RPI outputs. The RPI outputs are not completely understood and there is a need for more research.

This thesis presents four different studies.

The first study deals with experimental and numerical investigation of indentation on Cr(Mo)-NiAl eutectic alloy [4]. More specifically, the depth dependent strain partitioning between the layers of NiAl layered structure was measured using X-Ray microdiffraction. Finite element simulations were conducted to evaluate thermal strains due to cooling. Results from this simulation were further utilized to model microindentation of the eutectic composite. Strain data from simulations were compared with experimental results confirming experimentally observed trends.

The second study deals with simulation of RPI on bone. Bone was modeled as a material that exhibits elastic, plastic, viscous and continuum damage behaviors. The RPI process was simulated

as a cyclic indentation process using a finite element package Abaqus®. Effects of changing material properties, indentation force and number of cycles on the RPI outputs were evaluated computationally and compared with experimental works of similar nature and good coherence was demonstrated.

Third study presents a statistical approach to study the RPI outputs. Various mechanical tests (compression tests, stress relaxation test, tensile tests) were conducted on multiple 3D printed polymers and properties were obtained. These properties were analyzed against the RPI data of polymers in order to find correlations. The study is currently ongoing and data collected till date is presented in this thesis.

Fourth study presents a fast and efficient way of characterizing viscoelastic properties of soft materials based on experimental nanoindentation data and viscoelastic indentation tool on Nanohub [5]. PMMA (polymethyl methacrylate) was subjected to nanoindentation to obtain experimentally time-displacement data. This data along with experimental parameters (loading time, force and indenter radius) serve as inputs to the Nanohub viscoelastic simulation tool. This tool can provide 3 or 5 viscoelastic constants for materials, assuming a Standard Linear Solid model [6] for solids. Numerical data from simulations was matched against experimental data for two different loading rates and good match was observed.

ACKNOWLEDGMENTS

I would like to express my deep gratitude to Professor Iwona Jasiuk for her guidance and support. As an academic adviser, she guided my studies and provided valuable technical knowledge and encouragement. I would like to express my appreciation to Dr. R.I. Barabash, Prof. S. Koric, Dr. N. Sobh and Dr. T. Goudrazi for supporting my research.

I would like to thank Beckman Institute and Travis Ross for providing visualization facilities and Alexander Setters for technical support. Finally, I would like to thank my friends and family, who supported me in every endeavor of life.

TABLE OF CONTENTS

CHAPTER 1. GENERAL INTRODUCTION

NiAl based composites show great potential for high temperature applications (up to 1300^{o}C) in corrosive environments [4]. Strain partitioning is considered to be the prime reason for superior mechanical properties of these composites. Role of interfaces on strain partitioning has been emphasized by a number of authors [7-12] but the mechanisms of strain partitioning are still poorly understood. Chapter 2 of this thesis is based on the investigation of strain partitioning in Cr(Mo)-NiAl eutectic alloys. The study involves numerical simulations of experimentally measured strains across lamellae in Cr(Mo)-NiAl eutectic alloy. Finite element simulations were carried out to understand residual strains at the time of crystal formation and mechanically induced strains due to indentation. More specifically, contraction of material layers during cooling stage of crystal formation was modeled on finite element package Abaqus® and residual strains were computed. Substrate with residual strains was then used for an indentation study, where the substrate was indented with a spherical indenter. Strains resulting from indentation in addition to thermal strains were computed. Experimental measurements and numerical data showed good coherence.

Reference point indentation (RPI) is a novel indentation technique for evaluation of bone properties with the potential of being used in clinical setting [3]. In this technique, a reference probe sits on the surface while a test probe indents the bone surface multiple times. The device computes nine different parameters based on load-displacement measurement made during indentation. Currently, the outputs from RPI are not properly understood, thus, more research needs to be done. Chapter 3 presents a numerical study of the RPI where the indentation process is modeled on finite element package Abaqus®. Bone is modeled as a material that exhibits elastic, plastic, viscous and damage behaviors under indentation. Constitutive law for bone and model parameters were adopted from previous studies. Effect of variation of material properties and RPI

test settings were studied by numerical simulations and compared to experimental work of similar nature [13]. Various RPI outputs from simulations and their trends showed good coherence with experimental data.

Chapter 4 presents a statistical study with the objective to develop better understanding of RPI outputs. Better understanding of RPI outputs can be developed by correlating mechanical properties with RPI test measurements for multiple materials. 3D printed polymers were used as test materials for this study and were subjected to mechanical tests (compression test, stress relaxation test and tension test). RPI outputs for these parameters were available from another study [14]. Statistical correlations were investigated between mechanical properties and RPI outputs. The study is currently in progress and data available till date is presented.

Chapter 5 focuses on investigation of viscoelastic properties of soft materials in a fast and efficient way. Determination of viscoelastic parameters for soft materials is generally a complex and tedious task. The study demonstrates that viscoelastic parameters can be evaluated efficiently using nanoindentation test data and the viscoelastic simulation tool on Nanohub [5]. Two nanoindenation tests with different loading rates were conducted with PMMA as substrate and simulations were conducted using the viscoelastic simulation tool. Time-displacement data from experiments and simulations were found to match well. The demonstrated method should help researchers characterize biological tissues and other soft materials easily using this online tool.

CHAPTER 2. FINITE ELEMENT SIMULATION AND X-RAY MICRODIFFRACTION STUDY OF STRAIN PARTITIONING IN A LAYERED NANOCOMPOSITE

Abstract

The depth-dependent strain partitioning across the interfaces in the growth direction between the Cr and NiAl lamellae was directly measured experimentally and simulated using a finite-element method (FEM). Depth-resolved x-ray microdiffraction demonstrated that in the as-grown state both Cr and NiAl lamellae grow along the <111> direction with the formation of as-grown distinct residual ~0.16% compressive strains for Cr lamellae and approximately three times smaller tensile strains for NiAl lamellae. Three dimensional simulations were carried out using an implicit finite element method (FEM). First simulation was designed to study residual strains in the composite due to cooling resulting in formation of crystals. Strains in the growth direction were computed and compared to those obtained from the microdiffraction experiments. Second simulation was conducted to understand the combined strains resulting from cooling and mechanical indentation of composite. Numerical results in the growth direction of crystal were compared to experimental results confirming the experimentally observed trends.

2.1. Introduction

Strain partitioning is the most important phenomenon responsible for high mechanical properties of composites [7-12]. The role of interfaces on strain partitioning in composites was emphasized by a number of authors [15, 16]. In particular, Ni-based [9] and especially NiAl-based composites are the focus of current research because they can operate at high temperatures (up to 1300°C) in corrosive environments [17-24]. Therefore, they can be used for high temperature structural applications including structural components in energy conversion facilities. It was shown that small additions of Mo (up to 6 at%) change the morphology of the Cr phase from rod-like to

lamellar [25]. Therefore, NiAl/Cr(Mo) system has recently attracted attention because both phases grow into lamellae during crystallization [17, 18, 25-29]. However, the mechanism of strain partitioning in these alloys and the role of interfaces in load transfer from one phase to another are still poorly understood.

2.2. Materials and Experimental procedures

2.2.1. Growth of Cr(Mo)-NiAl Eutectic Alloys

The Cr-NiAl phase diagram has a eutectic point at a composition of 34 at% Cr at the temperature T_{eut} = 1450 °C. The eutectic temperature is lower than the melting temperature of Cr (T = 1880 °C) and of NiAl (T = 1674 °C) [20]. The NiAl/Cr alloys in this study were additionally alloyed by 3 at% Mo to obtain a lamellar structure of the composite. Cr(Mo)-NiAl samples were directionally crystallized with the formation of the well-aligned NiAl and Cr lamellae (Figure 2.1a). The details of the alloy preparation and eutectic growth can be found elsewhere [17, 18]. The spacing and relative size of lamellae depend on the growth rate and composition, and under the conditions of this experiment, resulted in approximately parallel lamellae with nearly equal thickness and a periodicity of ~1.2 μm. The sample was cut from a directionally solidified Cr(Mo)-NiAl eutectic rod perpendicular to the growth direction (cross-section), mounted in epoxy and then polished. Two kinds of samples were prepared: (1) in the first sample the matrix was etched away at the depth of ~5 micrometers – this sample was used to determine residual as-grown stresses in the lamellae; (2) the second sample was only slightly etched (several nm) to reveal the microstructure (Figure 2.1a). This sample was further indented and studied for strain partitioning between lamellae. The orientations of the lamellae along the growth direction were determined from the Laue pattern.

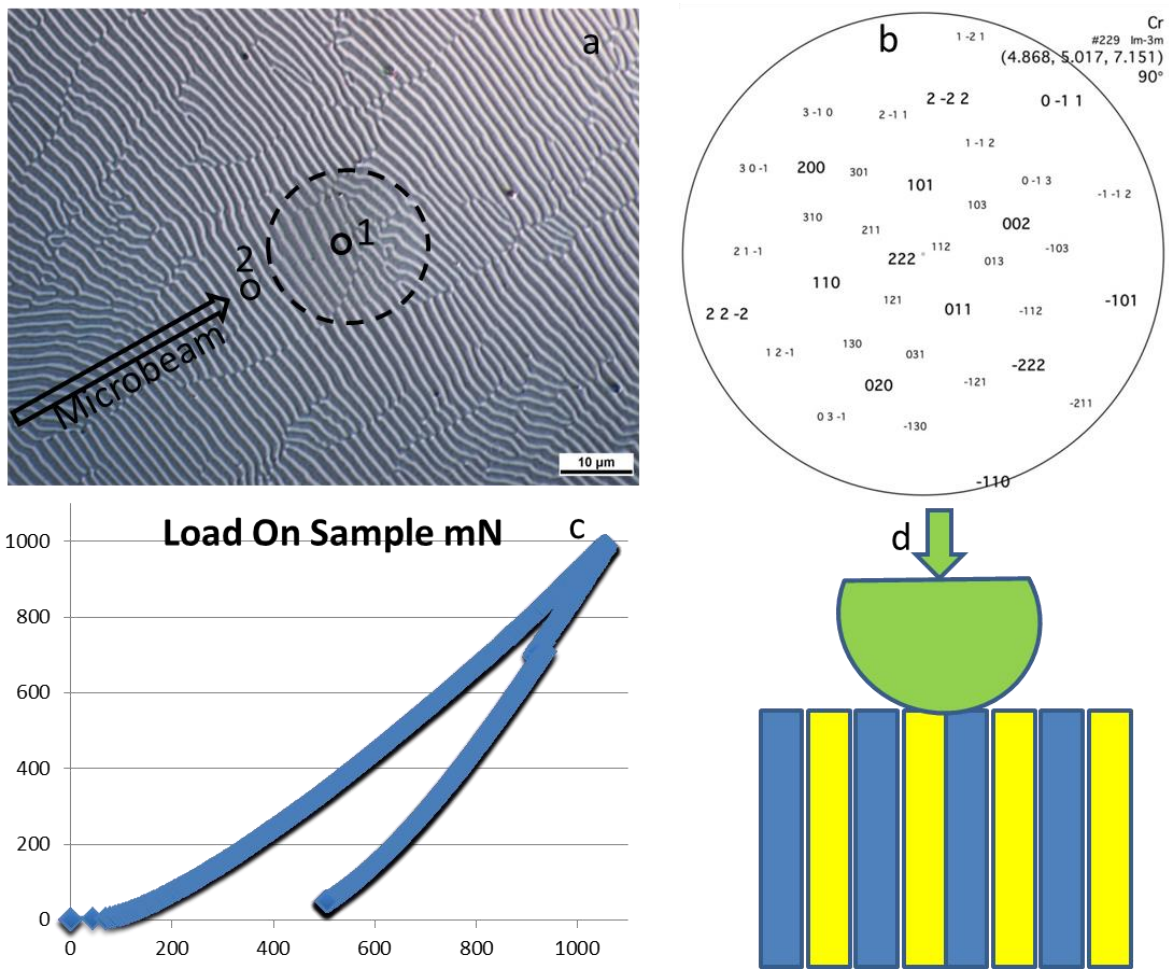

Figure 2.1: (a) SEM image of the indented area with Cr lamellae in NiAl matrix chosen for DAXM measurements. The direction of the beam trajectory intercepting the sample surface at 45° is shown by an arrow. Depth-resolved DAXM measurements of the indented sample were performed for locations 1 and 2. (b) Stereographic projection showing that growth is along <111> crystallographic direction; (c) Load-displacement curve during the indentation; (d) Sketch of the indentation along the lamellae growth direction.

The alternating Cr/NiAl lamellae are visible on the SEM image of the sample cross section (Figure 2.1a**).** The orientation of the surface normal was along the [111] direction for both Cr and NiAl lamellae.

2.2.2. Indentation

Spherical indentation on the polished surface perpendicular to the growth direction was conducted with an MTS Nano Indenter XP equipped with a sapphire tip with radius of 100 µm to a prescribed

load of P = 1,000 mN. Load-displacement curves were recorded for each indentation (Figure 2.1c).

2.2.3. Depth-Resolved X-ray Strain Microscopy

Polychromatic x-ray microdiffraction (PXM) was performed with a focused ~0.3 × 0.4 μm beam with an energy-dependent penetration depth ~30-50 μm. In this method, the x-ray microbeam intercepts the sample surface at ~45°. To obtain depth-resolved information about individual submicron-size lamellae, a differential-aperture x-ray microscopy (DAXM) technique was applied [18, 30-35]. DAXM technique can be performed using polychromatic (PDAXM) or monochromatic (MDAXM) radiation [35]. Both techniques allow obtaining information with 1 micrometer depth resolution. PDAXM reveals lattice orientation changes with depth, while MDAXM gives information about dilatational strain distribution with depth. Both PDAXM and MDAXM were used in the experimental study. These experiments were conducted by Dr. Rozaliya Barabash from Materials Science and Technology Division at Oak Ridge National Laboratory. They are summarized in Sections 2.2-2.3 for completeness.

2.3. Results and Discussion

2.3.1. Residual as-grown stresses

An SEM image of the cross section of the sample shows alternating Cr/NiAl lamellae with the total thickness of 1200 nm. The area of the indent is marked by a dashed circle. Stereographic projection obtained from undeformed region with PDAXM method (Figure 2.1b) unambiguously indicates that both kinds of lamellae grow along the [111] crystallographic direction. To get information about the possible as-grown residual strains, the depth-resolved inverse lattice parameters were measured with MDAXM in the first sample, where matrix was etched away at the depth of ~5 micrometers. The energy of the beam was scanned in the range corresponding to the (4, 4, 4) reflection with a step of 3 eV for both samples. The small x-ray beam size (< 0.5 μm)

allowed nondestructive measurements of lattice rotations and strains in the individual phase-specific mesoscale lamellae at different depths. The protruding out of the matrix Cr lamellae are strain/stress free. The beam coming at 45° to the sample surface is intercepting lamellae one-by-one as it penetrates the sample. It results in the plateau of intensity corresponding to the strain/stress free Cr(Mo) lamellae (Figure 2.2a). Initially, zero intensity diffracted from NiAl as the matrix is etched away. Therefore, no signal is observed in the area of etched matrix. Eventually, the beam is penetrating into the depth of the sample probing simultaneously Cr and NiAl lamellae. This relates to another plateau of intensity determined by the as-grown strained value of the d-spacing. Similar plateau of intensity is observed for NiAl at a different d-spacing. Line profiles corresponding to the two distinct depths are shown in Figure 2.2b. One depth corresponds to the near surface stress-free values for both lamellae kinds, while another depth corresponds to deep bulk values. The level of residual as-grown stresses estimated from the difference between these two values results in 0.16% compressive stress for the Cr lamellae and almost three times smaller tensile stress for the NiAl matrix.

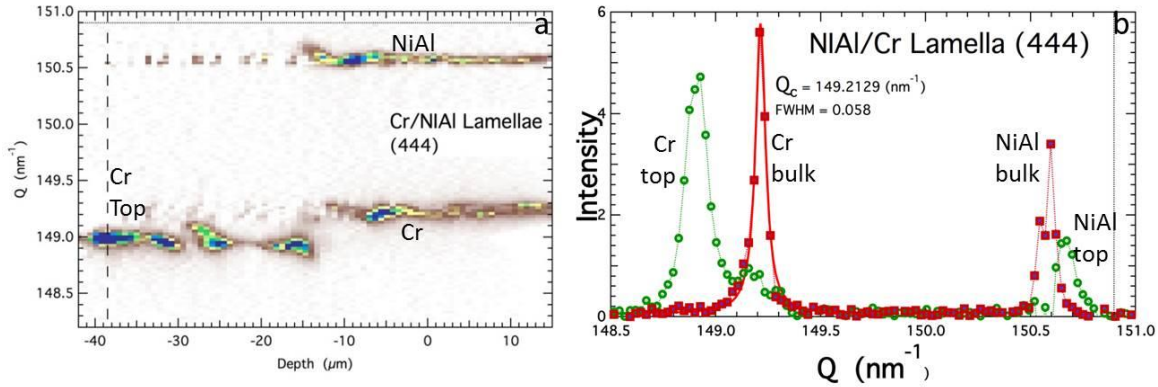

Figure 2.2: (a) Depth-resolved inverse lattice parameter Q_{444}-distribution measured in the energy interval for (444). (b) Line profiles corresponding to the stress-free NiAl and Cr lamellae at the surface (green open circles) and in the bulk of the composite (red filled squares); dashed vertical line in (b) is the relaxed theoretical value of the *d*-spacing.

2.3.2. Axial Texture

Strain partitioning was studied on the second sample without etching of the NiAl matrix. While both kinds of lamella grow along the [111] direction, an axial texture is observed in the cross section. It is visible both on the SEM image of the cross sections (Figure2.1a) and on the pole figure calculated from the white beam diffraction (Figure 2.3a). The in-plane direction of the lamellae colonies slightly varies from colony to colony. The axial texture also varies with depth which is indicated by a different color of the three-dimensional (3D) slice of the sample (Figure 2.3b).

The triple junction between the three colonies was chosen for indentation. The indented area was first mapped in 3D with depth-resolved white-beam measurements and the regions of largest deformation were found (Figure 2.3b). The probed area corresponds to the colony marked with purple color underneath the indent. In the most damaged near surface indented area the orientation of the affected lamellae changes stochastically and does not show any definitive orientation indicated by different colors.

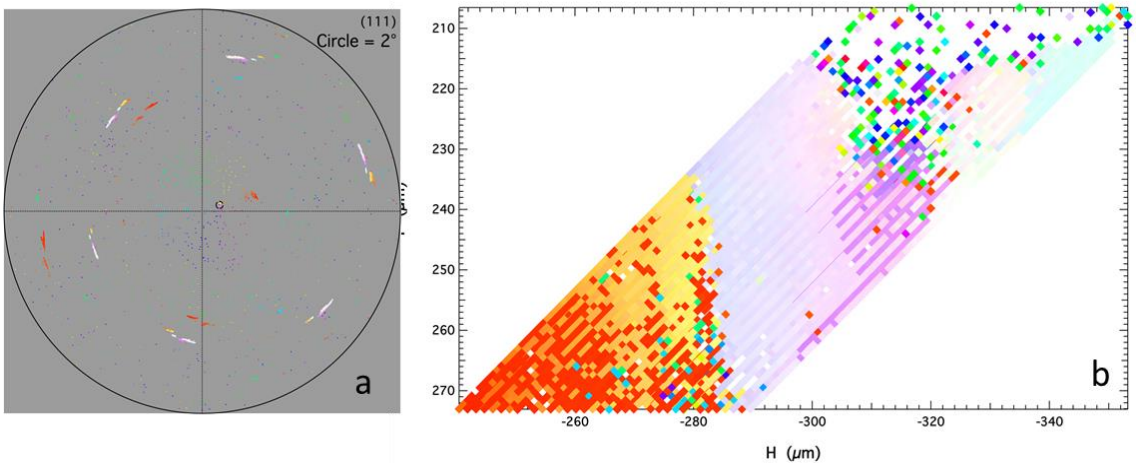

Figure 2.3: (a) Pole figure of the sample cross section shows sharp <111> texture; (b) Depth resolved 3D orientation map in the indented area.

2.3.3. Indentation-induced strain partitioning along the growth direction between the Cr and NiAl lamellae

Strain partitioning was characterized by 3D depth-resolved monochromatic measurements of the inverse (4, 4, 4) lattice parameter with the x-ray microbeam probing the sample along the two beam paths marked as (1) and (2) in Figure 2.1a. The measurement starting at the location 1 is taken in the most affected area while measurement starting at the location 2 probes mostly unaffected area and is used as reference.

The measured misfit between the two lamellae along the [111] growth in the strain-free near surface region is ~ 1.6%, while in the bulk of the composite it is ~ 0.86% due to residual strains.

Starting at location 1, the beam intercepts the sample surface in the area of largest deformation near the center of the indent (Figure 2.1a). Depth-dependent d_{444}-spacing measurements for Cr solid solution and NiAl lamellae (Figure 2.4a) demonstrate distinct signs and amplitudes of strain distributions between these two phases: the NiAl d_{444}-spacing decreases ~0.26% near the surface revealing that the near-surface deformed NiAl lamellae are slightly under compression. At the same deformed location the Cr lamellae are under tension compared to the bulk composite value for Cr: Cr lattice parameter in the affected region is 0.47% larger than in the bulk of the composite (Figure 2.4b). Tensile strains in the Cr lamellae first slightly increase with depth and reach their maximum value of ~0.54% at a depth of 6 μm, then the strain amplitude decreases, and at a depth of ~20 μm they saturate at their undeformed bulk values for both lamellae phases. The observation of distinct sign and amplitude strain distributions in the neighboring Cr and NiAl lamellae likely depends on the ratio between the elastic moduli of the Cr and NiAl neighboring lamellae and on the existing as-grown residual strains.

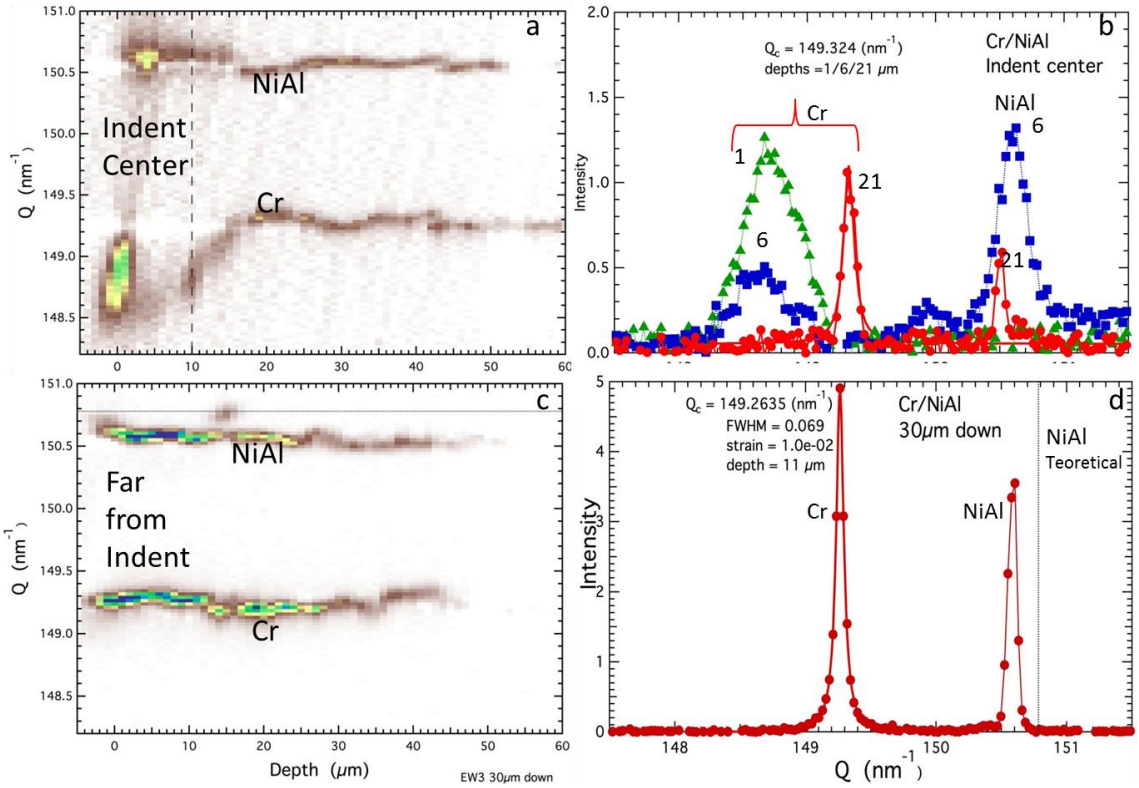

Figure 2.4 (a, b): Depth-resolved inverse [4, 4, 4] lattice *d*-spacing for beam path starting in location 1 in the center of the indented area (a) and corresponding line profiles at three distinct depths marked by numbers (b). (c, d) Depth-resolved inverse [4, 4, 4] lattice *d*-spacing for beam path starting in location 2 outside of the indented area (c) and corresponding line profiles (d) which practically do not change with depth.

2.3.4. Numerical Implementation and Computational Challenges: Simulation of indentation in NiAl-Cr composite

Finite element simulations were conducted in order to compute thermal strains and indentation induced strains in the NiAl-Cr composite. 3D numerical simulations were carried out with the implicit finite element method (FEM) using software Abaqus/Standard [36].

In order to perform a mesh refinement study, the domains were discretized using 20-node quadratic hexahedral elements with two levels of refinement, coarse and refined. The coarse mesh had more than 730,000 degrees of freedom (DOFs), while the refined mesh had almost 5 million DOFs.

Material nonlinearities from anisotropic plasticity along with geometric nonlinearities from large deformations and difficult contact conditions were accompanied with increased ill-conditioning due to element shape distortion in the mesh refinement, thus making a numerical analysis of the refined model extremely difficult even on the latest high performance computing platforms. Within each quasi-static time step, a system of nonlinear equations was linearized and solved with a Newton-Raphson (NR) iteration scheme [37, 38] in Abaqus which requires several linear solver solutions or global equilibrium iterations. The direct multi-frontal solver in Abaqus/Standard with hybrid parallelization was used. Koric et al [39] has recently showed that only this type of solver shows enough scalability and robustness to perform with large ill-conditioned problems on many hundreds of cores, while its hybrid MPI/Threaded implementation can take full advantage of large amount of memory and modern multicore processors. It is known that wall clock time for direct solution of sparse symmetric systems is approximately proportional to the square of the number of unknowns (or DOFs) [40]. While this is somewhat offset by a more efficient parallel execution on larger domains, it still imposes a severe restriction on the size of the domain that can feasibly be modeled with highly non-linear quasi-static problems even on the latest supercomputing platforms. Whereas the coarse mesh size takes 7 hours on 6 computational nodes (120 CPU cores), the refined case would require more than two weeks of dedicated supercomputer time on 15 computational nodes (300 CPU cores).

We used the High Performance Computing (HPC) cluster called iForge [41]. The iForge is at the National Center for Supercomputer Applications (NCSA) at the University of Illinois at Urbana-Champaign and is specifically built and tuned to accelerate some of the toughest industrial HPC workflows. The current configuration consists of 144 dual socket Dell PowerEdge M620 nodes,

each with two Intel Xeon E7 4890v2 CPUs (Ivy Bridge) and 20 cores operating at 2.8 GHz, and 256GB of RAM. They are connected with QDR Infiniband networking fabric.

2.3.4.1. Initial Thermo-Mechanical Simulations

Geometry used for simulation consisted of a rectangular block of dimensions 10 µm x10 µm x 5.6 µm. Alternating layers of NiAl and Cr layers, 0.8µm and 0.4µm thick, respectively, were modeled by partitioning the block into parallel layers, as shown in Figure 2.5. Layers were assumed to be perfectly bonded to each other and there was no possibility of delamination. The domain was meshed using cubic elements of size 0.1µm (Figure 2.5).

Layers were assumed to have cubic symmetry to match the experimental results and were given different anisotropic elastic properties, shown in Table 1. The z-direction in simulations corresponded to [111] direction for both crystal layers and was also direction of growth. The y-direction, which is the normal to the probed surface, was oriented along $[\bar{1}\bar{1}2]$. Local co-ordinate system was defined accordingly to provide direction specific elastic constants.

Thermal expansion coefficients were assumed to be constant over the temperature range used for simulations. Elastic moduli and thermal expansion coefficients are given in Table 1. Z-symmetry boundary conditions were applied to the model as the block was cooled down from 1400^{O}C to 0^{O}C.

Strains in the direction of crystal growth (along the z-axis) were the focus of analysis. It was observed that NiAl lamellae are under forward compressive stresses whereas Cr lamellae were under tensile back stress (Figure 2.6). Away from the boundaries, strains in both the layers were fairly uniform, giving a value of 0.19% in NiAl and -0.047% in Cr. The strains were visualized on the plane of symmetry of the model.

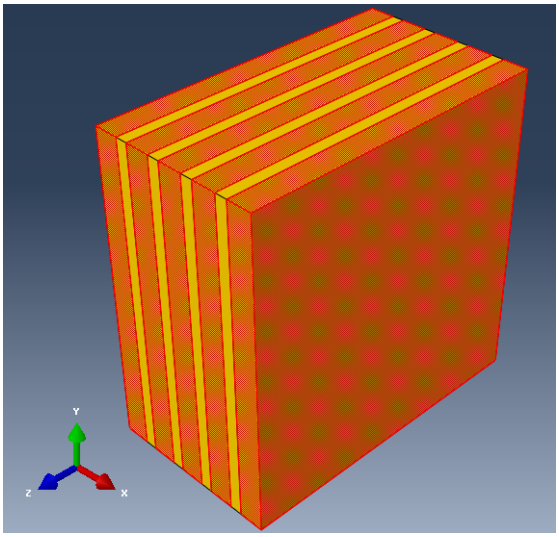

Figure 2.5: Geometry of the model used for finite element simulations.

Table 2.1 Elastic moduli and thermal expansion coefficients for NiAl and Cr lamellae

	c_{11} (GPa)	c_{12} (GPa)	c_{44} (GPa)	□(K^{-1})
NiAl	198	137	116	15.3 x 10^{-6}
Cr	350	68	101	4.9 x 10^{-6}

X-ray diffraction studies have suggested strain values of 0.1% and -0.025% in NiAl and Cr, respectively. It was observed that cooling the model in simulations from 700^{O}C to 0^{O}C yielded strain values very close to the experimental values.

2.3.4.2. Thermal simulation followed by indentation

From initial simulations, it was established that to obtain the residual strain state of NiAl-Cr, the finite element model should be run assuming cooling down by about 700^{O}C. A second simulation which included thermal and indentation steps was conducted. Residual thermal strains were generated by cooling the model by 700^{O}C, followed by indentation.

In the simulations, the geometry consists of two parts, composite cubic block with edge length 12 µm and indenter of radius 100 µm. Composite block had similar properties as adopted in the earlier model. Only a quarter of the block and indenter were modeled and symmetric boundary conditions were imposed (Figure 2.7). Direction of growth or the z-direction corresponds to [111] orientation for both crystals. Normal to the surface on which indentation was performed (y-direction) was oriented along $[\bar{1}\,\bar{1}2]$. Same elastic constants were adopted for the model as in the previous simulation and a constant yield stress of 200MPa was used for both materials to denote the unset of plastic deformation.

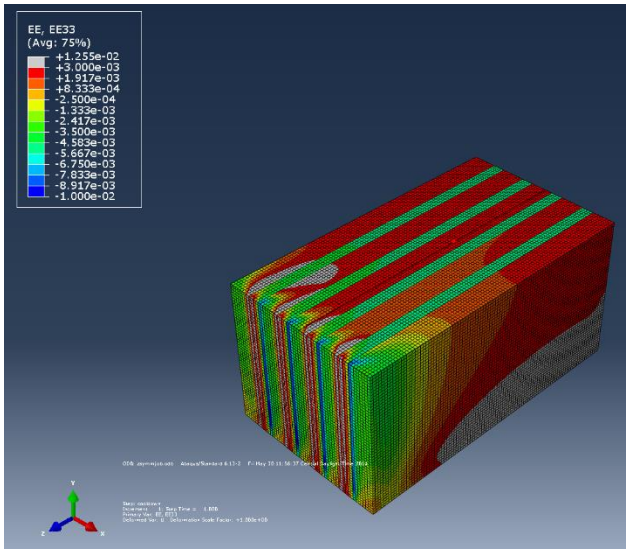

Figure 2.6: Simulated strains show that NiAl lamellae are under forward compressive stresses whereas Cr lamellae are under tensile back stress in agreement with experiment.

In the thermal step, the model was cooled down from 700^{O}C to 0^{O}C, followed by an indentation step, in which the indenter was pushed into the block by 1 µm at a constant velocity, followed by retraction of indenter at the same velocity.

As stated before, two different element sizes were used for meshing, 0.1 µm and 0.2 µm and results were analyzed. It was observed at the end of the thermal step as well as at 10% of the indentation

step that the coarser mesh resulted in very similar strain results as the finer mesh hence the problem was fully solved with a coarser mesh.

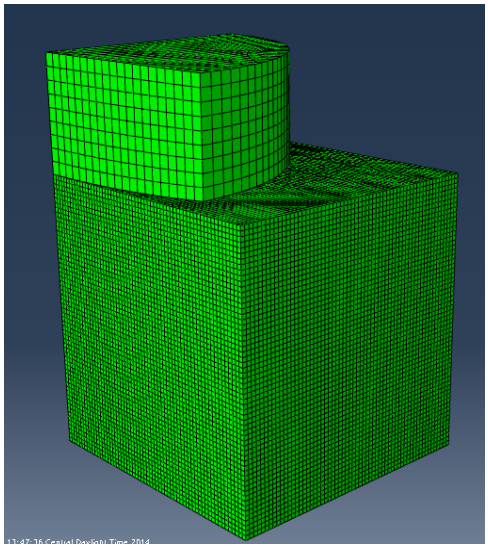

Figure 2.7: Model for thermal simulation followed by indentation.

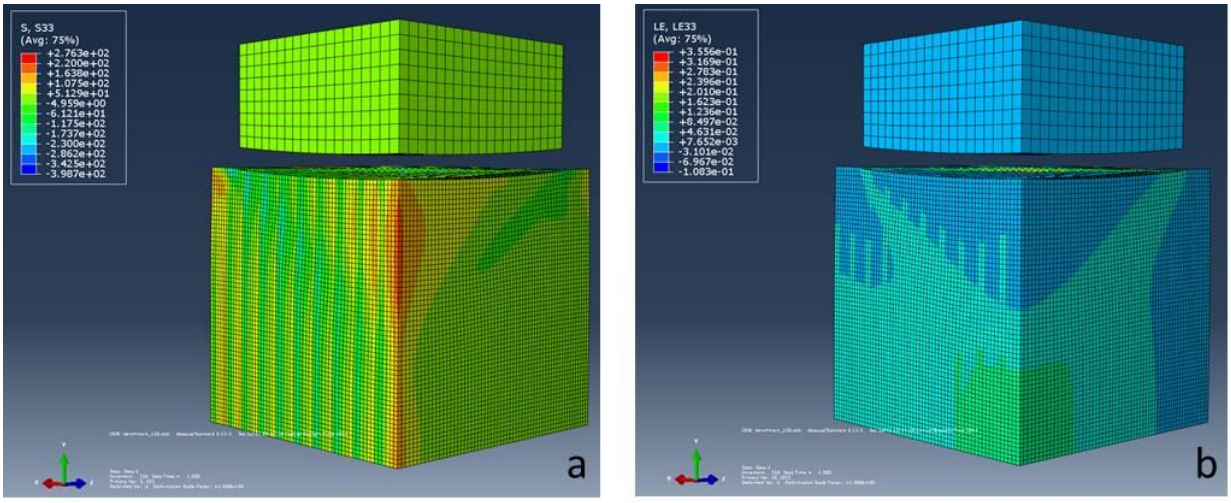

Figure 2.8: Simulated stresses along the growth direction. Simulations performed using different input parameters.

After cooling and indentation it was observed that NiAl and Cr lamellae were in different stress states as observed before. NiAl lamellae were under forward compressive stresses along the

direction of growth whereas Cr lamellae were under backward tensile stress (Figure 2.8) as compared to Figure 2.4a.

2.4. Conclusions

Indentation-induced strain partitioning between the individual lamellae results in alternating tensile/compressive strains in the submicron-size Cr and NiAl lamellae. Simulations confirm the experimentally observed alternating tensile/compression strains in the neighboring Cr and NiAl lamellae. Formation of these regions can be understood as a result of the compatibly constrained lamellae deformation and load partitioning through the interfaces between the harder and softer parts of the composite.

CHAPTER 3. FINITE ELEMENT SIMULATION OF REFERENCE POINT INDENTATION ON BONE

Abstract

Reference point indentation (RPI) [3] is a novel testing technique for evaluation of bone properties with a potential of being used in a clinical setting [42]. This technique utilizes cyclic loading to indent the substrate (bone) multiple times at the same point. Load-displacement response is recorded during indentation and post processed to calculate nine different parameters known as RPI outputs. The RPI outputs can potentially provide insights on bone quality and evaluate risk of bone fracture. However, the RPI parameters are not well understood by the scientific community as researchers continue conducting more experiments. This study aims at developing further understanding of the RPI parameters by using a computational approach. More specifically, bone is modeled on a commercial finite element software Abaqus™ by employing a material model that has been validated by accurately capturing bone's response under nanoindentation [43]. RPI cyclic indentation is simulated and the load-displacement response is computed. Post processing of load-displacement data yields the RPI parameters as calculated by the BioDent 1000™ RPI instrument (Active Life Scientific, Inc., Santa Barbara, CA). The RPI outputs are computed for different test cases where indentation load, number of cycles and material properties are varied. Trends in the RPI outputs with changing material property and testing conditions are presented and similarities with experimental results are examined. The RPI outputs related to creep and slope show good coherence with experimental trends observed by Setters and Jasiuk [13]. This computational study advances understanding of the RPI outputs and provides a starting point for more comprehensive computational studies.

3.1. Introduction

Multiple studies have been conducted to understand mechanical properties of bone using traditional materials testing, i.e. compression test, bending test and fracture toughness test [44][45][46]. The basic limitation of these testing methods are that they require large test samples, are *ex-vivo* and destructive. RPI technique was invented as an *in-vivo* testing technique to provide measurements of bone properties [3]. In the RPI technique, several indents are made at the same location on the substrate using a cyclic load (Figure 3.1) while monitoring load-displacement response. The load-displacement response is post-processed to calculate certain parameters known as RPI parameters. BioDent 1000™ Reference point indentation instrument (Active Life Scientific, Inc., Santa Barbara, CA) computes nine different RPI parameters, as listed in Table 3.1.

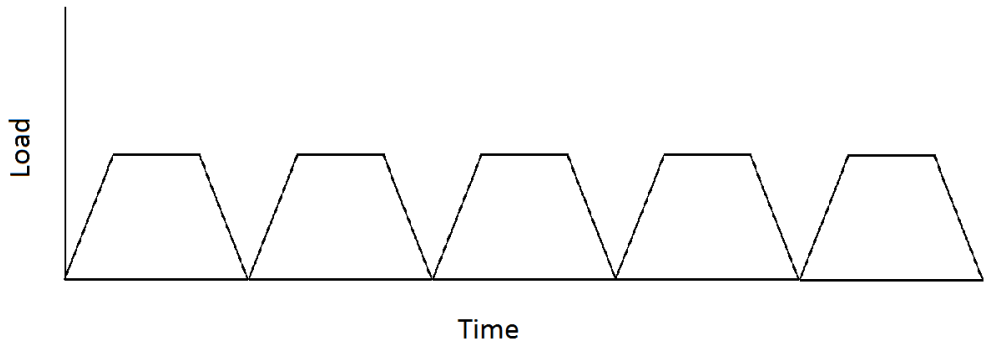

Figure 3.1:RPI load function for 5 cycles

ID1 and TID are maximum indentation depths after first and last cycle respectively. CID1 is the creep distance for the first loading cycle and AvCID is the average of creep distances over all cycles. US1 is the unloading slope for the first unloading and AvUS is the average of unloading slopes over all cycles. IDI is the increase in indentation depth observed between first and last cycles. AvLS is the average of loading slope over all cycles and AvED is the energy dissipated over the 3rd and last loading cycle. Figure 3.2 shows the first and last cycle response from a typical

load-displacement curves obtained from RPI. Note that Figures 3.1 and 3.2 illustrate a five cycle RPI test for visual clarity. The recommended number of cycles in the RPI test is 10-20 cycles.

Table 3.1: Description of RPI outputs

RPI Output	Description
ID1	Test probe penetration depth after first test cycle
US1	Unloading slope for the first test cycle
CID1	Creep indentation distance for first test cycle
TID	Total test probe penetration depth
IDI	Indentation depth increase from first cycle to last cycle
AvCID	Average of creep indentation depths over all cycles
AvUS	Average of unloading slopes over all cycles
AvLS	Average loading slope over all cycles
AvED	Average of energy dissipated over 3rd to last test cycle

In a previous study [47], IDI was found to be inversely correlated with bone material toughness obtained from 3-point bending and axial compression. IDI has been used as an indicator of bone properties in multiple studies. Rasoulin et al [48] studied age-related changes in porcine femoral cortical bone. Aref et al [49] demonstrated that raloxifene has positive effects on mechanical properties of bone following 6 months of treatments on dogs. Similarly, effects of glucocorticoid induced osteoporosis on bone properties was evaluated by Mellibovsky et al [50].

RPI parameters apart from IDI are underutilized by the research community as the meaning of these parameters is not yet clear. Thus, there is a need to develop better understanding of meaning

of these parameters and the properties they indicate before this technique can be used in clinical setting. This study addresses this need through a numerical approach.

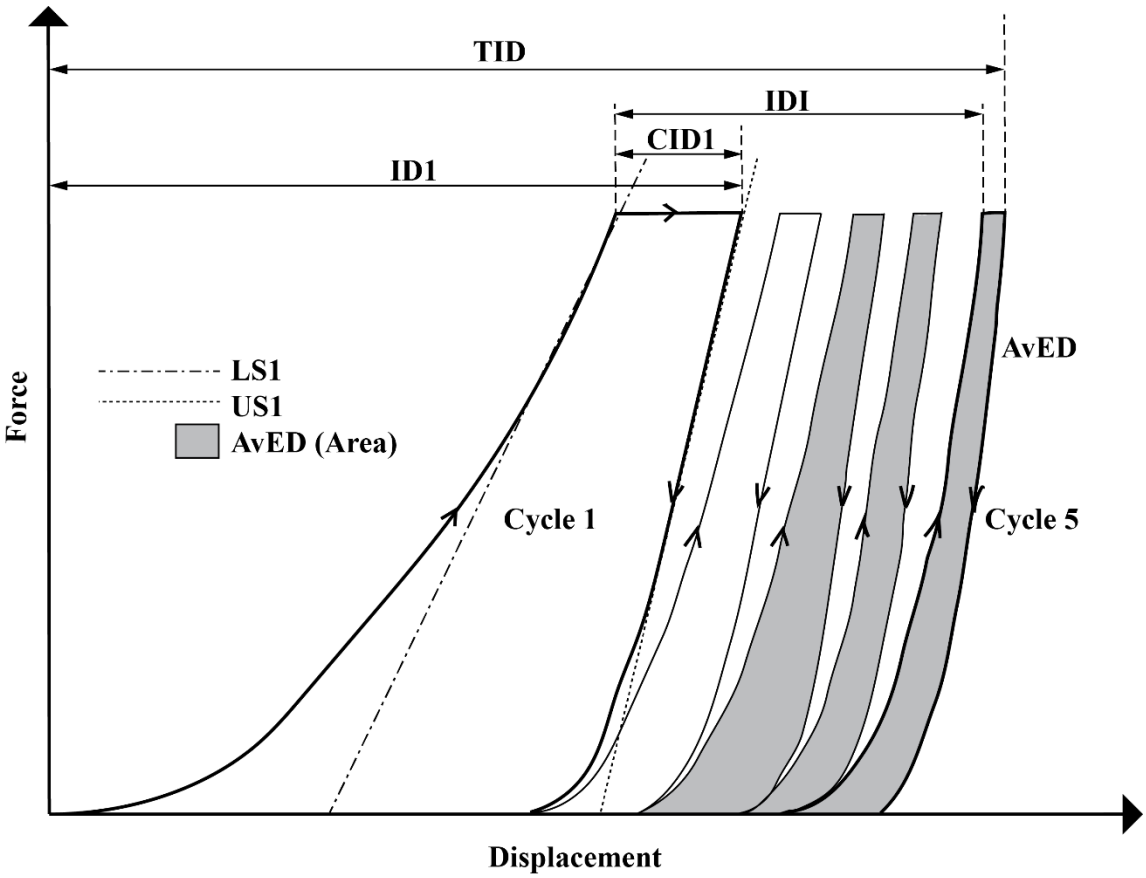

Figure 3.2: Plot showing typical RPI load-displacement curve and RPI outputs

Indentation processes (microindentation, nanoindentation) in engineering materials have been simulated by various researchers [51],[52],[53]. A constitutive law for bone was developed by Zhang et al [54], which accurately captured visco-elastic/plastic response of bone. Over subsequent years, Zhang et al developed a new model that captures not only visco-elastic/plastic behavior, but also continuum damage [43].

This study presents a simulation of RPI on Abaqus® using the material model for bone developed by Zhang et al [43]. The constitutive law depends on eight different material parameters, and four of those parameters (elastic modulus, yield stress, viscous parameter, damage parameter) were

varied and finite element simulations were carried out. Additionally, experimental parameters (peak load for indentation and number of cycles) were varied in simulations. Load-displacement response for each simulation was numerically obtained from simulations and post processed to calculate RPI parameters. Effects of input parameters on RPI outputs are observed and trends are compared to experiments conducted by Setters and Jasiuk [13].

3.2. Methodology

3.2.1. Material model

Plastic damage model of Lubliner et al. [55] is a general model that incorporates damage in materials and subsequent reduction in elastic modulus under tensile and compressive strains. Since tensile strains are negligible in indentation, damage due to tensile strains is neglected. Assuming linear kinematics, the strain tensor can be decomposed into elastic and plastic components

$$\varepsilon = \varepsilon^{el} + \varepsilon^{pl} \qquad \text{Eq 3.1}$$

Assuming continuum damage where d is the scalar damage variable, effective stress in the medium is given by Eq. (3.2).

$$\sigma = [1 - d]E^{el}{:}\,[\varepsilon - \varepsilon^{pl}] \qquad \text{Eq 3.2}$$

where E^{el} is elasticity tensor. Elasticity tensor is a function of elastic modulus E and Poisson's ratio ν for homogenous isotropic materials. True stress can be interpreted as stress resulting from undamaged area fraction $(1 - d)$ of the medium. The damage variable d assumes value between 0 (undamaged) and 1(fully damaged), depending on amount of damage induced by compressive strains. The damage parameter is related to plastic strain using an exponential function

$$d = \gamma(1 - e^{-\beta\varepsilon^{pl}}) \qquad \text{Eq 3.3}$$

where γ and β are parameters (refer to Table 3.2).

Elastic domain is defined by the yield function F as

$$F = \bar{q} - 3\alpha\bar{p} - Y \leq 0 \qquad \text{Eq 3.4}$$

where $\bar{p}$ is the effective hydrostatic pressure given by

$$\bar{p} = \frac{1}{3\bar{\sigma}} : I \qquad \text{Eq 3.5}$$

and $\bar{q}$ is the effective equivalent von-Mises stress given by

$$\bar{q} = \sqrt{1.5\bar{\sigma}^{dev} : \bar{\sigma}^{dev}} \qquad \text{Eq 3.6}$$

$\bar{\sigma}^{dev}$ is effective deviatoric stress.

Yield stress is expressed as

$$Y = [1 - \alpha]\bar{\sigma}_c - [\frac{[1 - \alpha]\bar{\sigma}_c}{\bar{\sigma}_t} - [1 + \alpha]]\langle\bar{\sigma}_{max}\rangle \qquad \text{Eq 3.7}$$

where $\bar{\sigma}_c$ is a uniaxial compressive failure stress, $\bar{\sigma}_t$ is a uniaxial tensile failure stress and $\bar{\sigma}_{max}$ is a maximum eigenvalue. In (3.6), $\langle 0\rangle = 0.5/[|o| + o]$ are Mcauley brackets, such that under plain compressive strain, second term vanishes and only first term remains.

Coefficient α is given by

$$\alpha = \left[\frac{\sigma_{b0}}{\sigma_{c0}} - 1\right] / [2\frac{\sigma_{b0}}{\sigma_{c0}} - 1] \qquad \text{Eq 3.8}$$

where σ_{b0}/σ_{c0} is the ratio of equibiaxial compressive yield stress to uniaxial compressive yield stress.

Non-associated plastic flow for bone is defined by a plastic potential G as

$$G = \bar{q} - \bar{p}.\tan\psi \qquad \text{Eq 3.9}$$

where ψ is a dilation angle, $\bar{p}$ is the effective hydrostatic pressure and $\bar{q}$ is the effective equivalent von-Mises stress as described in Eq. (3.5) and Eq. (3.6)

Model also implements a Duvaut-Lions type visco-plastic regularization for equivalent plastic strains $\kappa_c$and κ_t and scalar damage variable d.

$$\dot{d}^{vp} = \left[d - d_{vp}\right]/\mu \qquad \text{Eq 3.10}$$

$$\dot{\kappa}_c^{vp} = \left[\kappa_c - \kappa_c^{vp}\right]/\mu \quad \text{Eq 3.11}$$

$$\dot{\kappa}_t^{vp} = \left[\kappa_t - \kappa_t^{vp}\right]/\mu \quad \text{Eq 3.12}$$

where μ is a viscosity parameter.

The parameters and their default values used in this study as inputs to Abaqus® model are shown in Table 3.2.

Table 3.2: Material parameters and values for bone

Parameter	Value	Description
$\boldsymbol{\psi}$	22.5^o	Dilation angle
$\frac{\boldsymbol{\sigma_{b0}}}{\boldsymbol{\sigma_{c0}}}$	1.125	Ratio of equibiaxial compressive yield stress to uniaxial compressive yield stress.
$\boldsymbol{\sigma_{c0}}$	100 MPa	Uniaxial compressive yield stress
$\boldsymbol{E}$	18.6 GPa	Elastic modulus
$\boldsymbol{\nu}$	0.3	Poisson's ratio
$\boldsymbol{\gamma}$	0.9	Constant for calculation of d using (3.3)
$\boldsymbol{\beta}$	19	Constant for calculation of d using (3.3)
$\boldsymbol{\mu}$	0.04 s	Viscosity constant

The parameters E, σ_{c0}, γ and μ were varied one at a time, keeping all other properties constant and simulations were conducted. Values used for E, σ_{c0}, γ and μ are shown in Table 3.3.

3.2.2. Geometry and mesh

A two dimensional axisymmetric model was used to efficiently simulate conical indenter, as illustrated in Figure 3.3. Conical indenter has a 45^o half angle and substrate is a cylinder of radius

Table 3.3: Material parameters variation

Constant	Values
$\boldsymbol{E}$	16 GPa, 17 GPa
$\boldsymbol{\sigma_{c0}}$	50 MPa, 75 MPa
$\boldsymbol{\gamma}$	0.5, 0.8
$\boldsymbol{\mu}$	0.02 s, 0.08 s

2 mm and height 2 mm. Size of substrate is about 100 times larger than indentation depths ($\sim 20\mu m$). Biased meshing with smaller elements close to the indentation zone was used. Element size close to indenter was 5 μm and 50 μm on bottom far corner. Mesh consists of mostly quadrilateral elements and had some triangular elements, totaling to about 40000 elements in the block (Figures 3.3 and 3.4). Tip of the indenter is slightly rounded using a curvature of 30 μm.

3.2.3. Boundary conditions

Motion of bottom of block was restricted in the vertical direction and pressure load was applied on the top of indenter. Surface to surface frictionless contact algorithm was used to model contact between indenter and substrate. Biodent instrument operates at 2Hz frequency and Figure 3.6 shows one cycle of the load function. The instrument can be operated at five different force settings (2, 4, 6, 8 and 10N) and different number of cycles (5,10,15,20). In this study, three different forces (6, 8 and 10N) were used and three different number of cycles were used (5, 7 and 10 cycles).

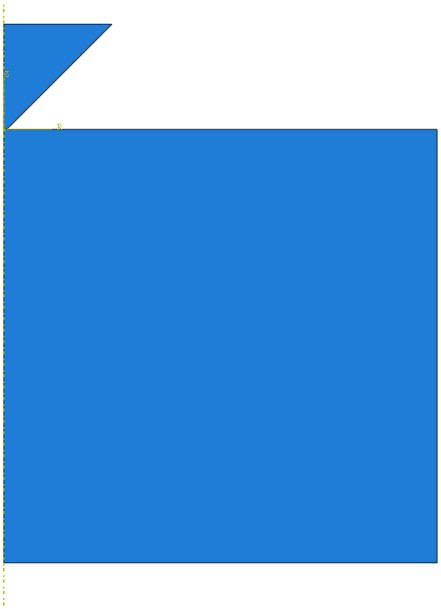

Figure 3.3: Geometry for FE simulation

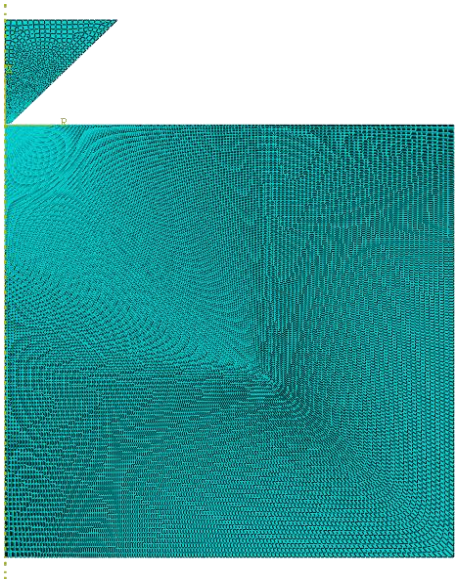

Figure 3.4: Mesh for FE simulation

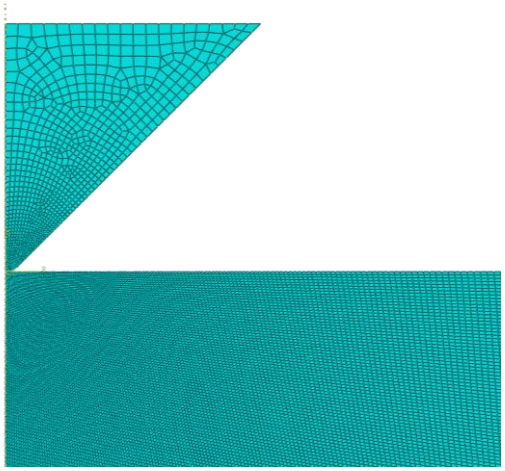

Figure 3.5: Mesh near Indenter

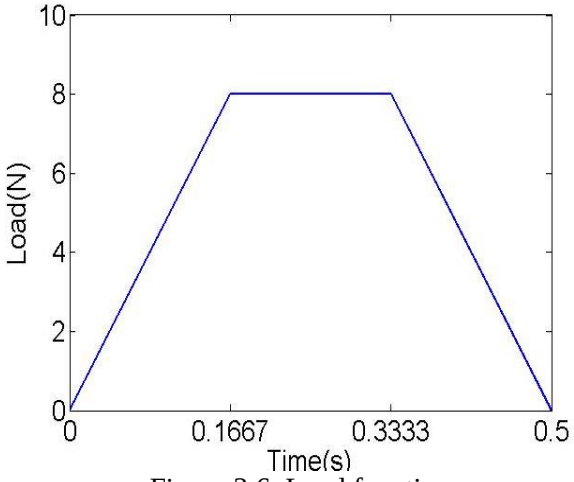

Figure 3.6: Load function

3.2.4. Convergence of solution

RPI uses a sharp conical indenter, which results in high strains that are difficult to simulate using a finite element method. To ease this problem of convergence, the tip of indenter was rounded off slightly with an arc (R = 30 μm). It is expected that round tip will result in lower indentation distances in general, but overall trends shouldn't be affected.

3.2.5. Post-processing

Load-displacement response of substrate was obtained from simulations and RPI parameters were computed from the load-displacement data. Typical time-displacement response is illustrated in Figure 3.6 and load-displacement plot is shown in Figure 3.7. Figure 3.7 also graphically illustrates outputs ID1, TID and IDI (descriptions provided in Table 3.1). BioDent® calculates unloading slopes by fitting a line to data points between 5% and 40% of unloading time interval. Loading slopes are calculated by fitting a line to data points obtained in the last 40% of the loading time interval.

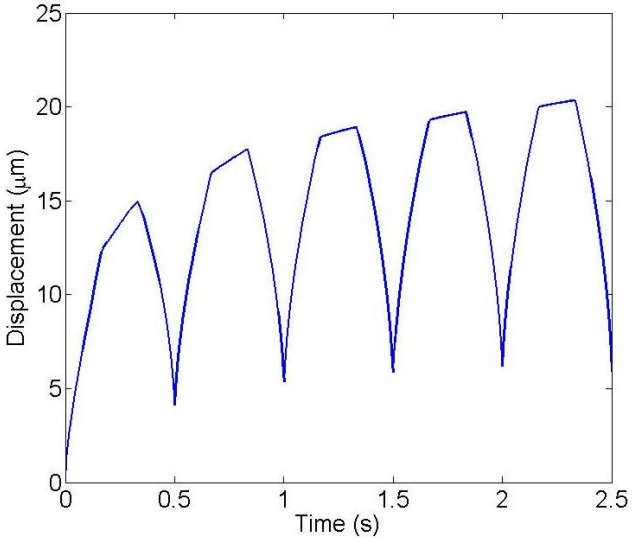

Figure 3.7: Typical Displacement time response

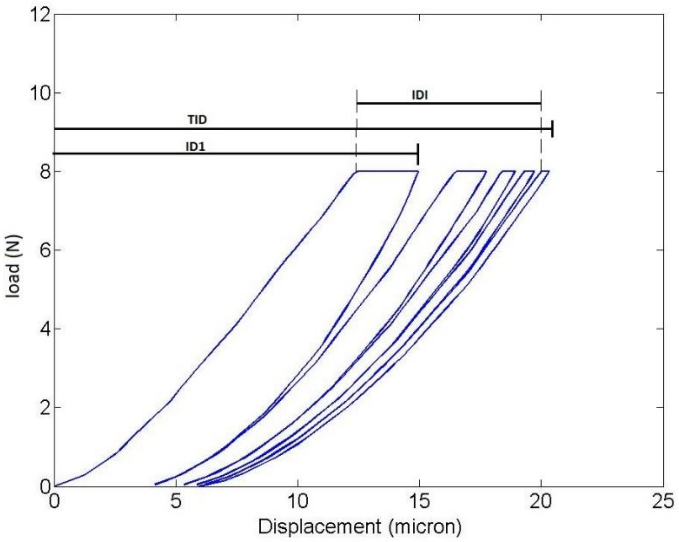

Figure 3. 8: Typical load-displacement response

3.3. Results

Figure 3.9 shows the value of scalar damage parameter d after 5 load cycles. Figure 3.10 illustrates von-Mises stresses in the model, at the peak load for last cycle.

It is evident from contour plots that damage is contained within a very small zone close to the indenter (~50 – 100 μm). Highest stress values (~1.6GPa) are observed close to the indenter tip.

Figures 3.11 and 3.12 show effects of variation of elastic modulus and yield stress. Material becomes more compliant as elastic modulus and yield stress are decreased and indentation depths are higher.

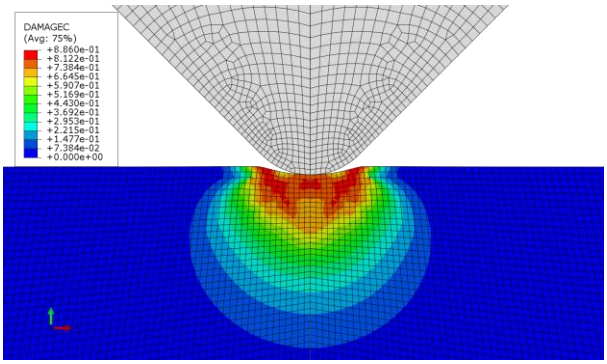

Figure 3.9: Contour plot of scalar damage parameter d

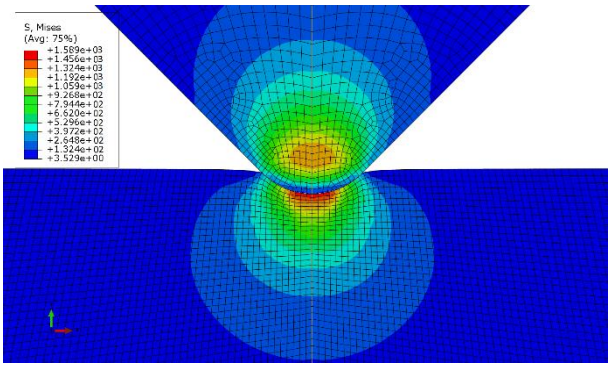

Figure 3.10: Contour plot of von Mises stresses (MPa)

Figure 3.13 shows effects of variation of the damage parameter, increase in damage parameter results in deeper indents. Figure 3.14 shows effects of variation of the viscous parameter. Lower viscous parameter results in low viscous stresses hence higher creep distances. Figure 3.15 illustrates the effect of different peak loads, higher peak loads result in larger indentation distances. RPI parameters are extracted from load-displacement curves and shown in Table 3.4.

Decrease in elastic modulus, yield stress, viscous parameter and increase in damage parameter correlates with increase in indentation distances (ID1, TID and CID).

A strong correlation between US1 and elastic modulus is observed (R^2 value of 0.9987) which shows that US1 can be used as a measure for determining elastic modulus.

We observed that US1 remains unchanged with varying compressive yield stress as material response close to start of unloading was mainly elastic.

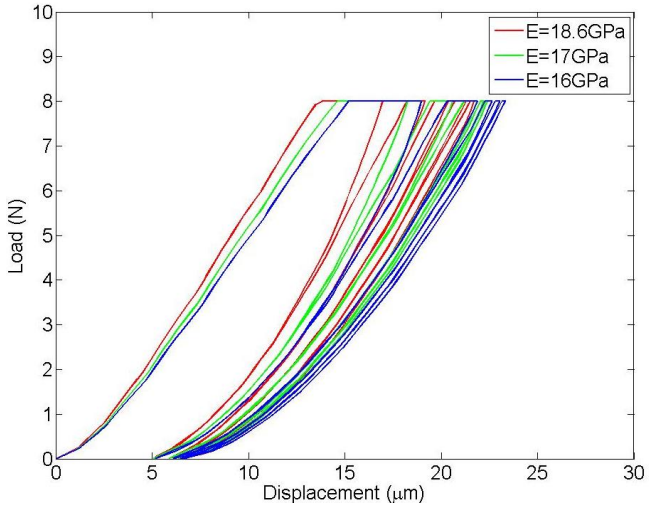

Figure 3.11: Effect of elastic modulus

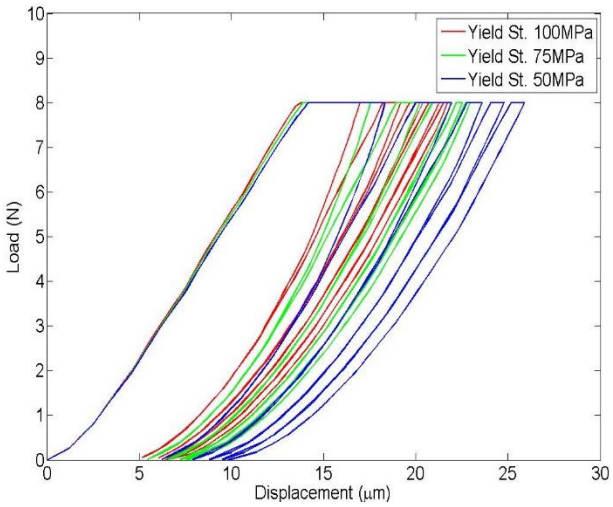

Figure 3.12: Effect of Yield Stress

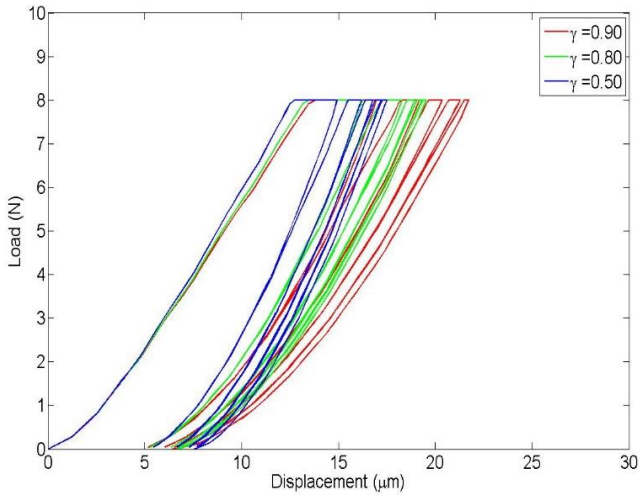

Figure 3.13: Effect of Damage parameter

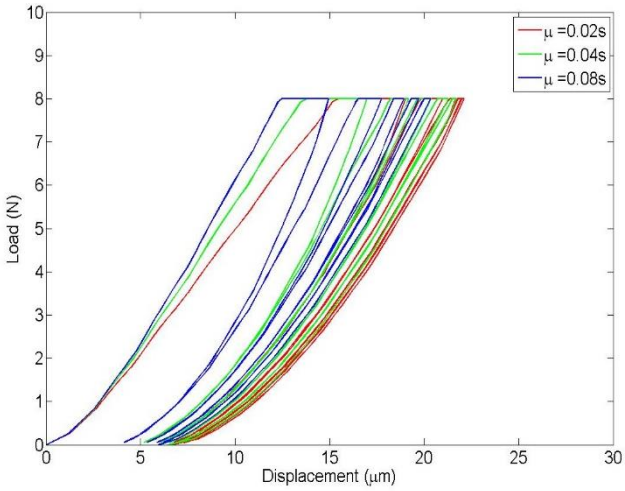

Figure 3.14: Effect of Viscous parameter

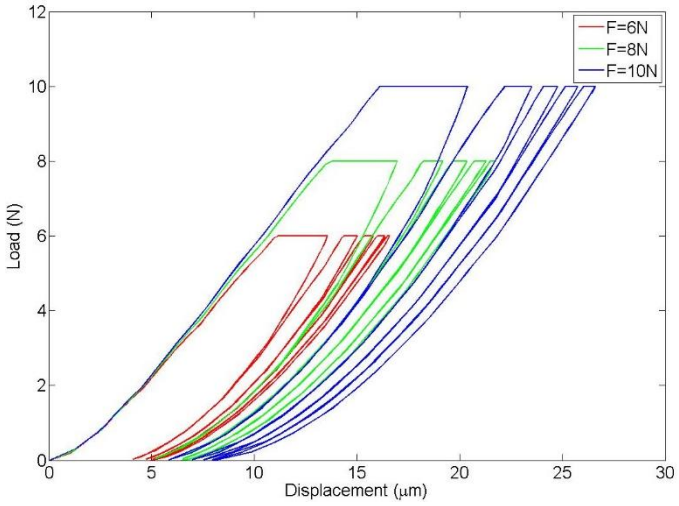

Figure 3.15: Effect of Load variation

AvUS did not change with change in yield stress, indicating that yield stress has little effect on AvUS. The AvLS however changes with change in yield stress, and might be used for characterizing plasticity. Unloading slopes (both US1 and AvUS) were also affected by change in damage parameter, force and viscous parameter.

IDI was not a strong function of elastic modulus, but varies highly with damage parameter and yield stress. Average loading slope trends were same as average unloading slope and were always slightly less than Average unloading slope. Creep distances (CID1 and AvCID) increases were correlated with decrease in elastic modulus, yield stress, viscous parameter and increase in damage parameter.

3.3.1. Comparison with experiments

Computational results were compared with experimental work of Setters and Jasiuk [13], where they report effects of changing load and cycles on RPI parameters. It is difficult to match the indentation distances as in this numerical study the indenter had a slightly rounded tip. This artifact

Table: 3.4: RPI outputs as computed from simulations

	ID1 (μm)	CID1 (μm)	TID (μm)	IDI (μm)	AvCID (μm)	US1 (N/μm)	AvUS (N/μm)	AvLS (N/μm)
Default properties	16.95	3.13	21.72	7.68	1.10	1.05	0.85	0.77
E=16 GPa	18.97	3.77	23.32	7.96	1.21	0.88	0.75	0.70
E=17 GPa	18.23	3.61	22.42	7.68	1.15	0.94	0.78	0.73
σ_{c0} =50 MPa	18.30	4.13	25.89	10.98	1.66	1.06	0.84	0.73
σ_{c0} =75 MPa	17.52	3.63	22.95	8.81	1.30	1.06	0.84	0.75
γ =0.50	14.92	2.18	17.50	4.53	0.75	1.15	1.15	1.04
γ =0.80	16.24	2.75	19.54	5.89	0.90	1.06	0.93	0.87
F=6 N	13.56	2.40	16.58	5.32	0.79	0.94	0.80	0.75
F=10 N	20.36	4.25	26.61	9.92	1.48	1.10	0.90	0.82
μ =0.02	19.01	3.50	22.11	6.49	1.03	0.88	0.78	0.73
μ= 0.08	14.94	2.45	20.34	7.53	0.98	1.08	0.90	0.85
7 cycles	16.95	3.14	22.17	8.25	0.82	1.03	0.82	0.77
10 cycles	16.95	3.14	22.48	8.62	0.59	1.03	0.80	0.78

made the tip blunt and naturally reduces the indentation depths. However, one could observe trends of RPI outputs while varying load and number of cycles.

3.3.1.1. Force Variation

The results for different forces are summarized in Table 3.5. Increases in ID1 and TID with increase in force were observed experimentally and computationally. In both computational and

experimental results reported in [13], it was observed that US1, AvUS, AvLS, CID1 and AvCID increase with increase in load. Comparison between experimental and computational results are presented in Figures 3.16 a-d.

Table 3.5: RPI outputs obtained from simulations for different force setting

	ID1 (μm)	**CID1 (μm)**	**TID (μm)**	**IDI (μm)**	**AvCID (μm)**	**US1 (N/μm)**	**AvUS (N/μm)**	**AvLS (N/μm)**
F=6 N	13.56	2.40	16.58	5.32	0.79	0.94	0.80	0.75
F=8 N	16.95	3.13	21.72	7.68	1.10	1.05	0.85	0.77
F=10 N	20.36	4.25	26.61	9.92	1.48	1.10	0.90	0.82

3.3.1.2. Cycle Variation

Results for cycle variation are presented in Table 3.6.

Both experiments and simulations suggest that ID1, TID, US1, AvUS and CID1 didn't vary much with changing number of cycles. With increase in cycles, however, a significant decline is seen in AvCID (Figure 3.17a). This was attributed to decrease in creep distances with every consecutive cycle as observed in load-displacement curves (Figures 3.11-15). A sharp increase in IDI (Figure 3.17b) was seen in both experiments and computations for lower number of cycles (2 and 5), the increase becomes gradual for higher number of cycles (7, 10 and 15).

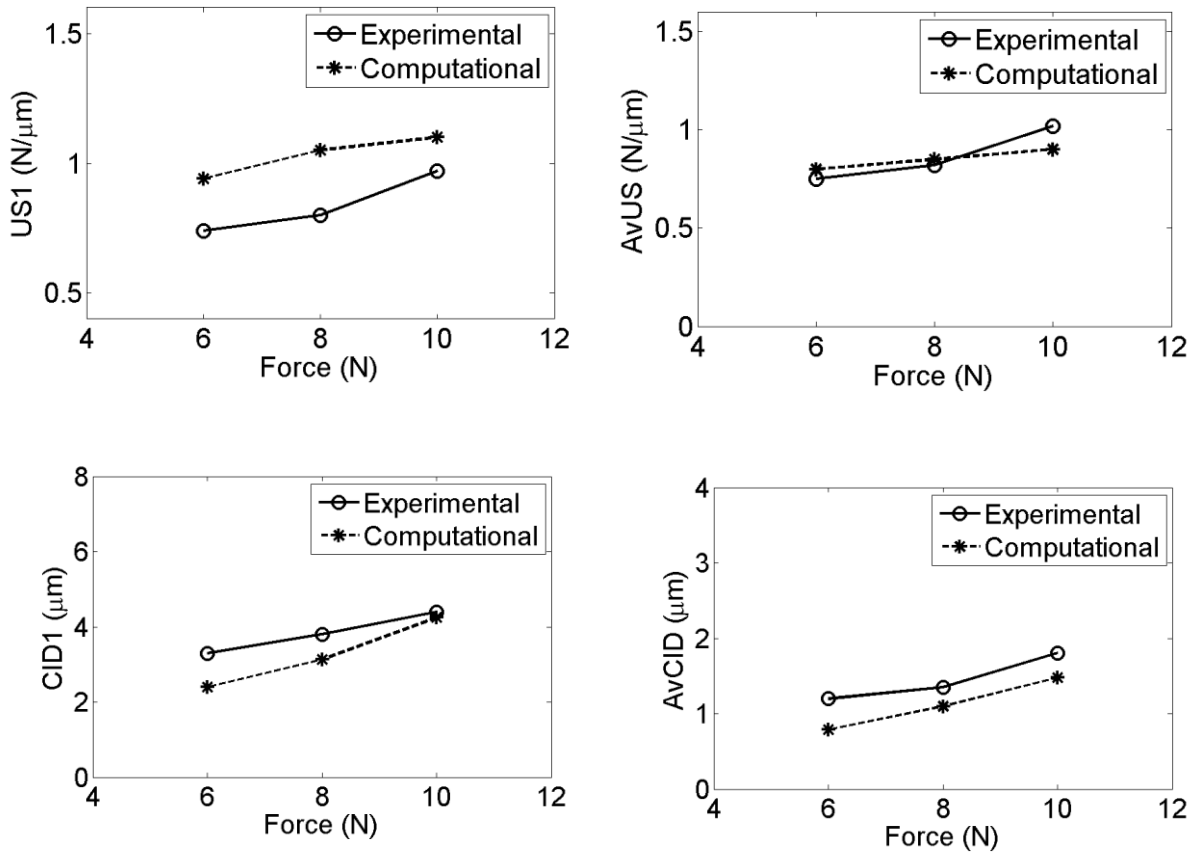

Figure 3.16: Comparison between experimental and computational results for a)First Unloading slope, b) Average Unloading Slope, c) Frist Cycle Creep Distance, d) Average Creep Distance

Table 3.6: RPI outputs as computed from simulations for varying number of cycles

	ID1 (μm)	**CID1 (μm)**	**TID (μm)**	**IDI (μm)**	**AvCID (μm)**	**US1 (N/μm)**	**AvUS (N/μm)**	**AvLS (N/μm)**
2 cycles	16.95	3.13	19.16	4.43	2.02	1.05	0.85	0.74
5 cycles	16.95	3.13	21.72	7.68	1.10	1.05	0.85	0.77
7 cycles	16.95	3.14	22.17	8.25	0.82	1.03	0.82	0.77
10 cycles	16.95	3.14	22.48	8.62	0.59	1.03	0.80	0.78

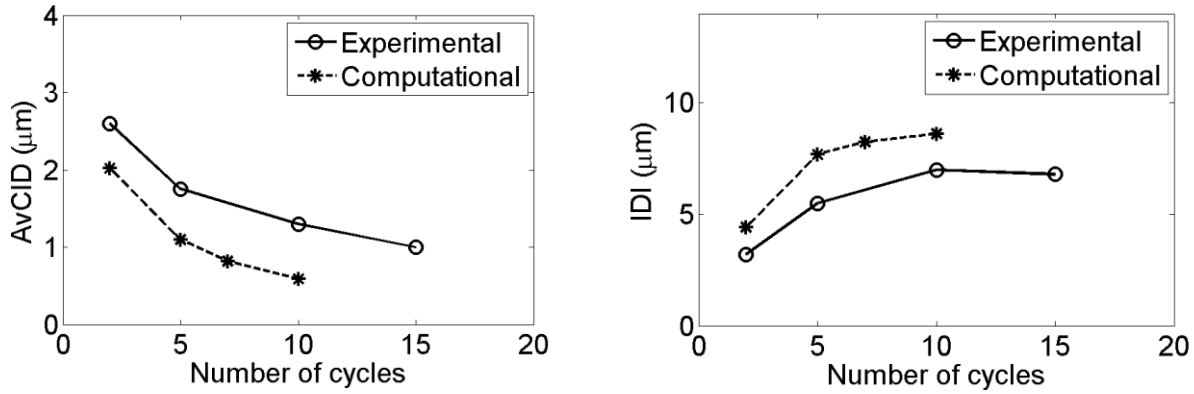

Figure 3.17: Comparison between experimental and computational results for

a) Average Creep Distance, b) Indentation Depth Increase

3.4. Conclusion

Finite element simulations successfully simulated Reference Point Indentation and they provide new insights on how the RPI parameters are related to parameters describing a constitutive law of bone. Data from simulations were found to be in accordance with similar experimental studies. The IDI increases with increase in damage in bone. Unloading slopes were found to be a good indicator of elastic modulus. Plastic properties (compressive yield stress) were found to affect AvLS, which is otherwise very similar to AvUS. Experiments [13] as well as simulations suggest that with increase in loading force, CID, AvCID, US1 and AvUS increase. With increasing number of cycles, AvCID and IDI were found to decrease.

This study has several limitations. The constitutive law used [43] implements a continuum damage model and didn't model cracks explicitly and did not account for failure of material. On the contrary, scanning electron microscopy images [43] of substrate subjected to RPI showed cracks. Moreover, this study regarded bone as a uniform isotropic material, whereas it is known that bone

has a complex microstructure and exhibits anisotropy. Future studies should account more precisely for inhomogeneity and anisotropy of bone and crack initiation and propagation.

Simulation provided new insights into the RPI technique. Further insight can be obtained by more realistic simulations and further experiments using the RPI technique. Such studies are needed before the RPI method can be used in clinical setting.

CHAPTER 4. RPI STUDY OF POLYMERS

4.1. Introduction

Chapter 3 of this thesis presented a computational approach to develop understanding of Reference Point Indentation (RPI) outputs. This study proposes a statistical approach towards the same goal. Comparing mechanical properties with RPI outputs for multiple polymers will provide better understanding of RPI outputs.

Polymers made using 3D additive manufacturing processes are the materials used for this study (Table 4.1). Polymer blocks were subjected to conventional mechanical tests (uniaxial compression test, tension test and stress relaxation test) to determine material properties. RPI outputs for the polymers were available from previous works of Setters [14].

Compression tests can provide mechanical properties like elastic modulus, yield stress and plastic behavior. Stress relaxation tests can give viscoelastic properties and tensile tests can provide properties like elastic modulus, yield stress, plastic properties, toughness and ultimate tensile strength of polymers. We intend to carry out all these tests in future and compare data against RPI outputs for the materials. For the purpose of this thesis, results available till date i.e. data from compression test and stress relaxation test are presented.

4.2. Methods

4.2.1. Compression Test

Polymer blocks of eight different polymers (size 20 mm x 10 mm x 10 mm) were created at Rapid Prototyping Laboratory in the Department of Mechanical Science and Engineering at the University of Illinois. The polymers were subjected to compression tests on Instron® Model 4483 load frame at Mechanical Testing Instructional Laboratory, University of Illinois. Three different

strain rates: 0.01% /s, 0.1%/s and 1%/s were used for testing of each material. Load-displacement data were processed to obtain stress-strain data.

Table 4.1: 3D printers and materials

Machine	Materials
Fortus 360MC	ABS, PC, PC ABS
Viper SI Stereo Lithography Apparatus	Protogen White, WaterClear Ultra
Eden 350 (Objet Geometries Ltd.)	Fullcure, Vero White
Formiga P100 Selective Laser Sintering	PA 2200

4.2.2. Stress Relaxation Test

Polymer blocks (size 20 mm x 10 mm x 10 mm) were also subjected to stress relaxation tests on Instron® Model 4483 load frame at Mechanical Testing Instructional Laboratory, University of Illinois. Load was ramped up to attain 3% strain and then crosshead was stopped and polymers were allowed to relax. Decrease in load with time was recorded and used to calculate stress-strain data and decrease in stress with time.

4.3. Results

4.3.1. Compression Test

Compression test data for different polymers are presented in Figures 4.1a-g. We can clearly observe that stress-strain data are different for different strain rates. For most polymers, stress-strain curves for low strains coincide, but as the strain increases, samples subjected to higher strain rates exhibit higher stresses. This type of behavior is attributed to the viscoelastic nature of polymers.

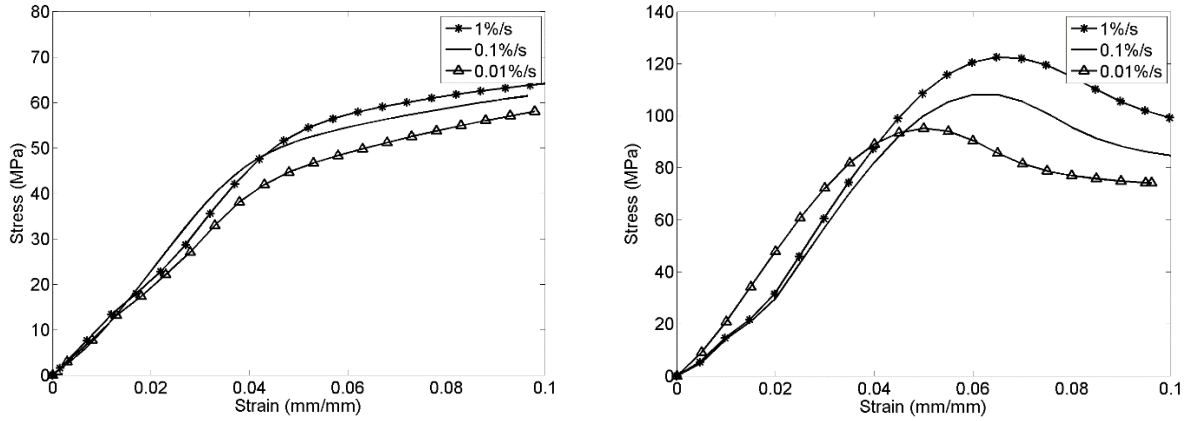

Figure 4.1a,b : Stress-strain curves for PA2200 (left) and Protogen White (right)

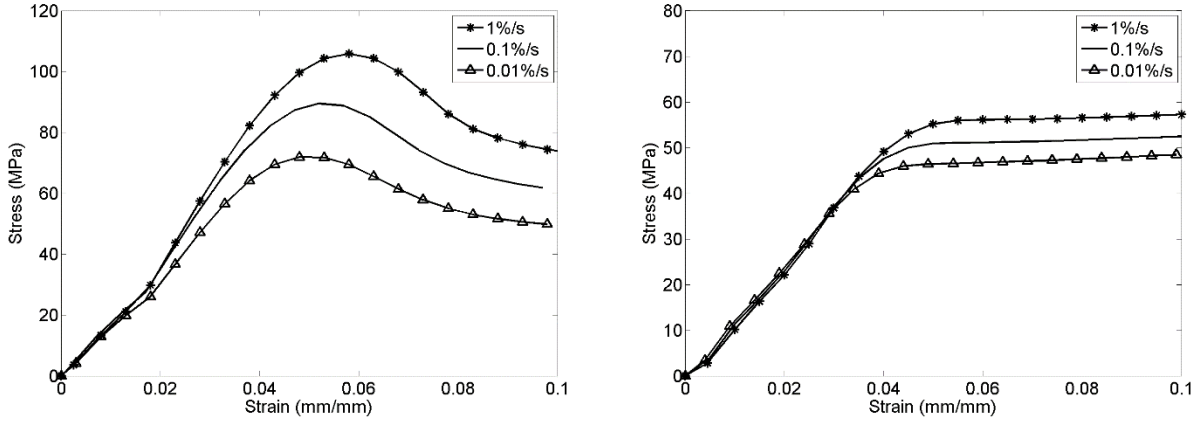

Figure 4.1c,d : Stress-strain curves for Waterclear Ultra (left) and ABS (right)

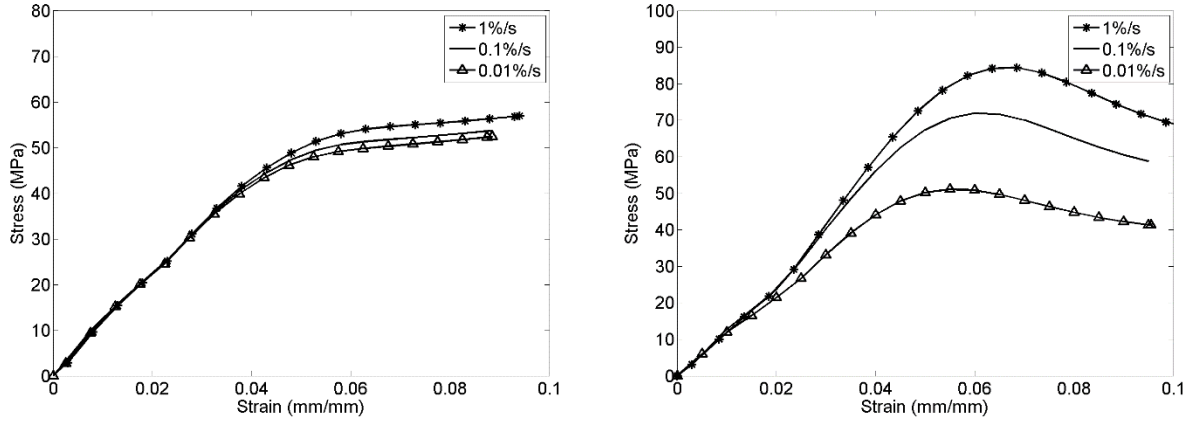

Figure 4.1e,f : Stress-strain curves for PC (left) and Fullcure (right)

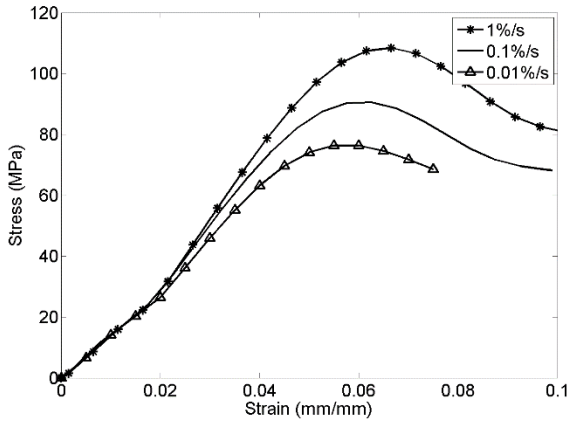

Figure 4.1g : Stress-strain curves for Vero White

It was observed that some polymers exhibit more strain rate dependent behavior than others. The stress-strain curves for PC and ABS are very close together for different loading rates, suggesting less viscoelastic behavior.

4.3.2. Stress Relaxation tests

Figures 4.2a-h present stress-strain curves for initial loading part of stress relaxation curves.

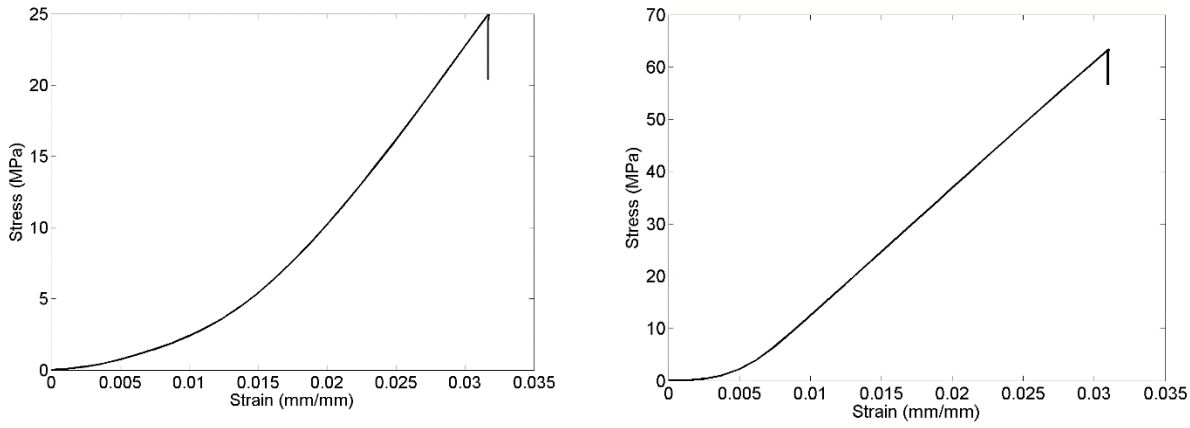

Figure 4.2a,b : Stress-strain curves for PA2200 (left) and Protogen White (right)

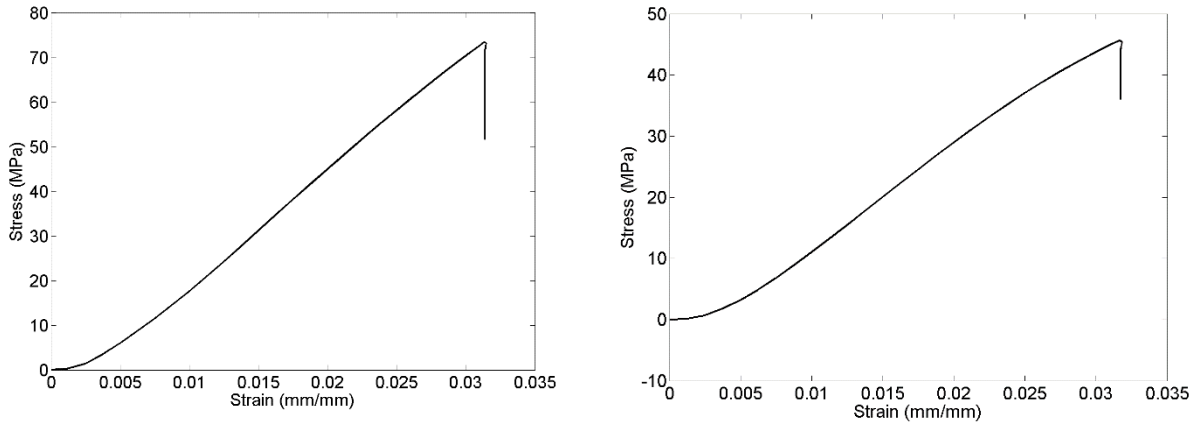

Figure 4.2c,d : Stress-strain curves for Waterclear Ultra (left) and ABS (right)

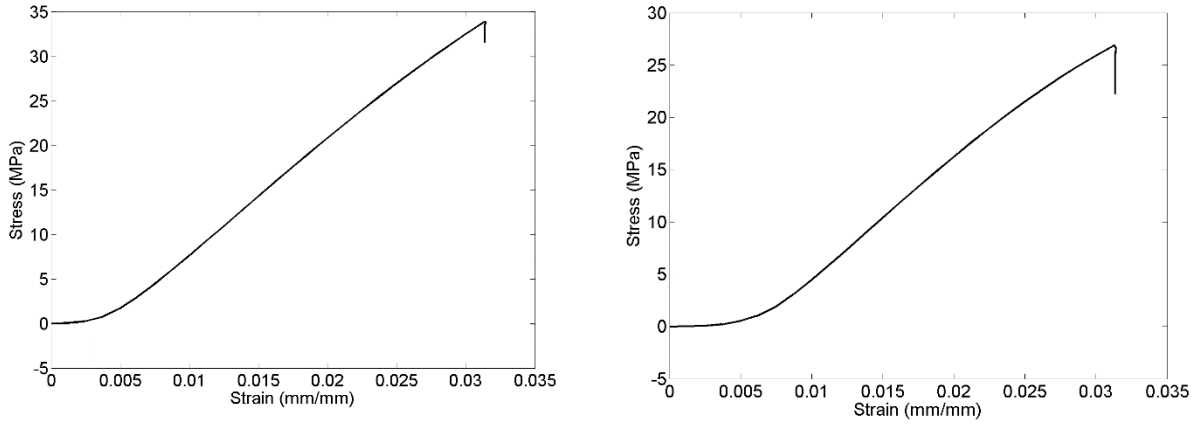

Figure 4.2e,f : Stress-strain curves for PC (left) and PC ABS (right)

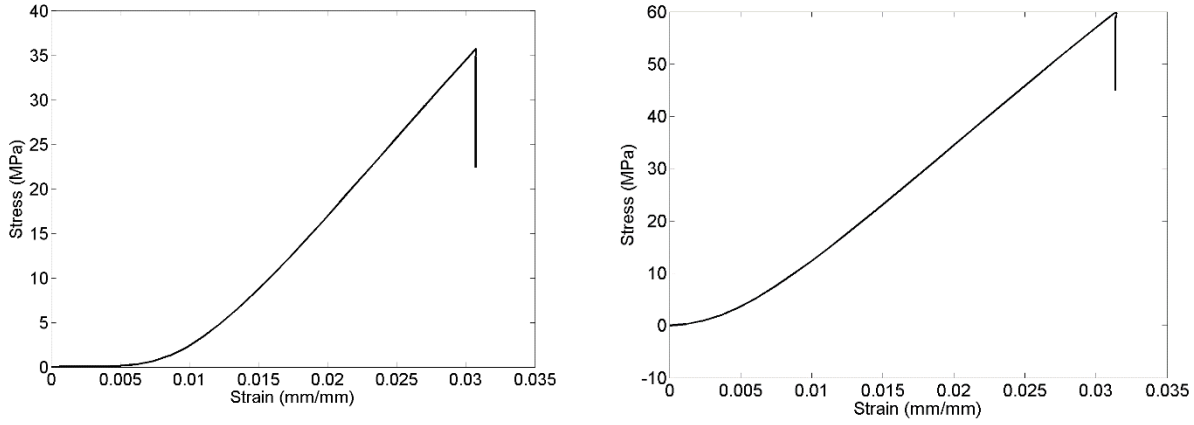

Figure 4.2g,h : Stress-strain curves for Fullcure (left) and Vero White (right)

Figures 4.3a-h present stress relaxation data with time.

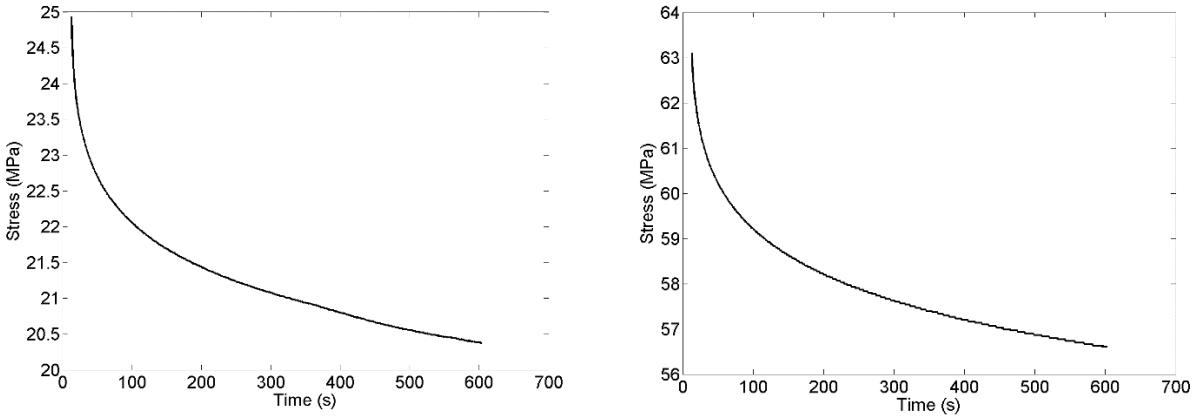

Figure 4.3a,b : Stress-strain-curves for PA2200 (left) and Protogen White (right)

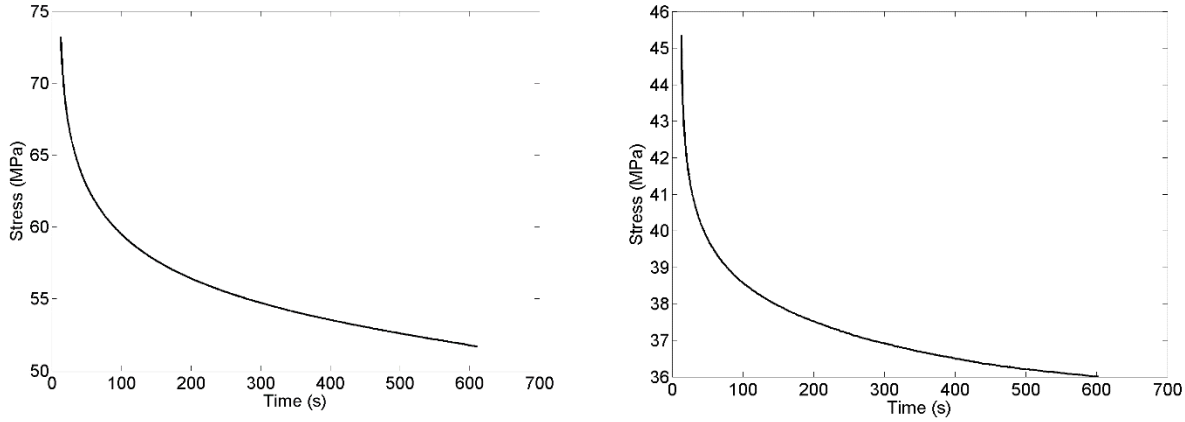

Figure 4.3c,d : Stress-strain curves for Waterclear Ultra (left) and ABS (right)

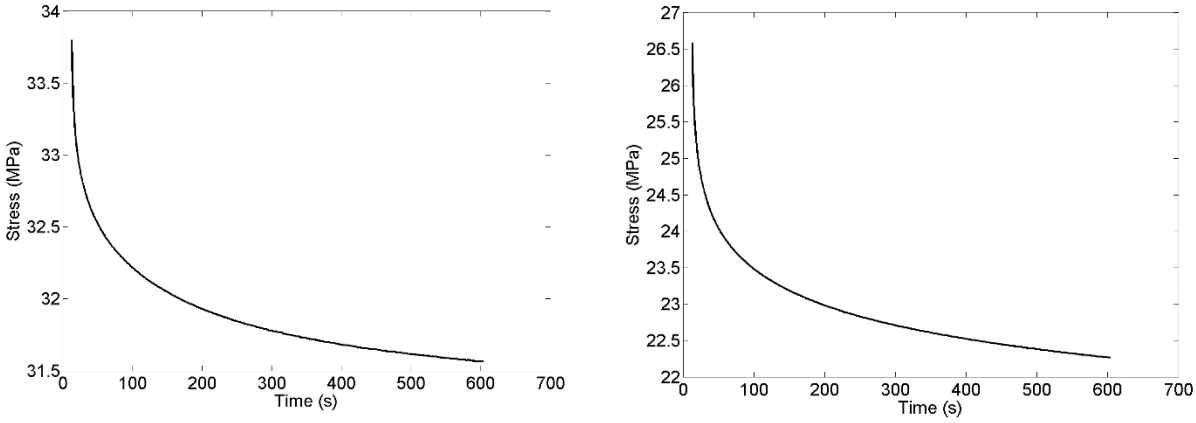

Figure 4.3e,f : Stress-strain curves for PC (left) and PC ABS (right)

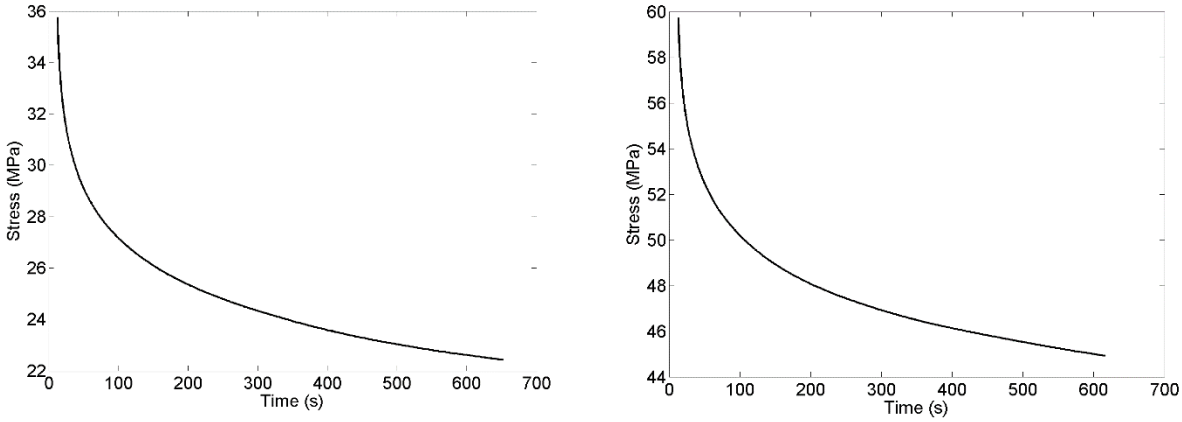

Figure 4.3g,h : Stress-strain curves for Fullcure (left) and Vero White (right)

4.3.3. Data Analysis

Yield stress for slowest loading rate was calculated from compression test data. Initial compression data from stress relaxation test was used to compute elastic modulus. Stress relaxation data was used to compute two parameters, ratio of highest and lowest stress value and time constant, assuming decay of stress to be of exponential nature. Calculated data and elastic modulus data from polymer data sheets is presented in Table 4.2.

Table 4.2: Calculated data for various polymers

Material	Time constant (s)	Stress ratio $\left(\frac{\sigma_{max}}{\sigma_{min}}\right)$	Elastic modulus from Compression (GPa)	Yield Stress (MPa)	Elastic modulus from data sheets (GPa)
PA2200	86.50	1.224	1.17	45	1.65
Protogen White	94.50	1.121	2.43	89	2.25
Waterclear Ultra	82.44	1.422	2.63	69	2.88
ABS	44.31	1.267	1.61	43	
PC	50.95	1.073	1.22	43	2.3
PC ABS	41.46	1.208	1.05		1.9
Fullcure	87.00	1.595	1.74	48	2.5
Vero White	81.87	1.331	2.27	74	2.5

Elastic modulus data found from experiments did not match well with elastic moduli values from data sheets. 3D printing involves deposition of material in layers to form parts, which results in a composite polymer structure, which might be responsible for this mismatch.

Table 4.3 presents the RPI outputs for the polymers obtained from works of Setters [14]

Correlations between results from Table 4.2 and Table 4.3 are presented in Table 4.4 using a cut-off $p < 0.05$ for significant result.

It is observed that yield stress correlates with ID1 and TID inversely, similar to the trend observed in numerical simulation of RPI in Chapter 3. Stress ratio showed significant correlation with US1, AvUs and AvLS. Time constant correlates with ID1 and TID and shows a negative correlation with US1 and AvUS.

Table 4.3: RPI outputs for polymers

Polymer	ID1 (µm)	US1 (N/µm)	CID1 (µm)	TID (µm)	IDI (µm)	AvCID (µm)	AvED (µJ)	AvUS (N/µm)	AvLS (N/µm)
ABS	83.000	0.364	5.600	87.000	8.260	1.620	25.400	0.398	0.258
FullCure 720	61.000	0.414	5.000	63.200	6.180	1.460	19.000	0.462	0.318
PA2200	63.600	0.428	5.000	66.800	7.520	1.600	19.020	0.478	0.338
PC	87.600	0.366	7.200	92.600	11.560	1.460	16.940	0.402	0.332
PC-ABS	76.600	0.334	5.000	81.000	8.100	1.660	26.640	0.376	0.268
PMMA	86.000	0.326	6.400	89.600	9.100	1.660	22.740	0.370	0.282
Proto Gen White	71.400	0.446	7.000	78.400	12.740	1.960	19.060	0.494	0.372
Vero White	66.200	0.404	6.200	70.800	9.540	1.900	22.940	0.458	0.320
Waterclear Ultra	54.400	0.492	5.000	58.000	8.200	1.460	12.560	0.526	0.428

4.4. Discussion

Preliminary results indicate various correlations between mechanical properties and RPI outputs. In future, tensile tests will provide more inputs like toughness which will be analyzed against the RPI outputs. Studies on bone have suggested a correlation between toughness and IDI [47], which may be observed in polymers too.

Table 4.4: Correlations for polymers

Correlated variables	P value	Correlation
Yield stress and ID1	0.010	-0.87
Yield stress and TID	0.005	-0.90
Stress ratio and US1	0.041	0.73
Stress ratio and AvUS	0.046	0.72
Stress ratio and AvLS	0.020	0.79
Time constant and ID1	0.027	0.76
Time constant and US1	0.022	-0.78
Time constant and TID	0.037	0.74
Time constant and AvUS	0.025	-0.77

This study treats 3D printed polymers as isotropic, which might not be the true case. 3D printed objects are created layer by layer, which might introduce microstructure and anisotropy in the material. For future studies, we intend to make measurements along different directions to ensure a more comprehensive dataset. Such data could also prove valuable for researches working on 3D printing, the RPI technique and these polymers.

CHAPTER 5. MODELING OF VISCOELASTIC MATERIALS

5.1. Introduction

Various researchers have demonstrated that diseased tissue can be distinguished from healthy tissue by analyzing mechanical properties [56]-[57]. Biological tissue often exhibits viscoelasticity and quantification of this behavior is often complex and tedious. Consequently, researchers are attempting to characterize tissue properties using various contact techniques (nanoindentation, reference point indentation) and non-contact techniques (using magnetic resonance, ultrasound, optical coherence). In this study, we will illustrate a fast and efficient way to characterize viscoelastic properties of soft materials using nanoindentation data and viscoelastic simulation tool on Nanohub [5].

Nanoindentation experiments on PMMA were conducted using two different ramp loads (10 s and 100 s) and material response was monitored continuously. Raw data obtained from one of the experiments (100 s ramp time) was processed to obtain time-displacement data. This data was supplied to viscoelastic simulation tool as input along with experimental parameters i.e. indenter geometry, load and ramp time. Outputs from the simulation tool were analyzed and validated against the other experiment (10 s ramp time).

5.2. Methodology

5.2.1. Nanoindentation

PMMA samples were obtained from Active Life Scientific, Inc., Santa Barbara, CA. PMMA was sliced into 3 mm thick samples and mounted on metallic fixtures using glue. The sample was polished using fine grit sandpapers - P180, P280, P400, P800, P1200, P2400, and P4000, followed by micron cloth/powder combinations of 1 mm/1 mm, 0.25 mm/0.3 mm, and 0.25 mm/0.05 mm.

PMMA was tested on Hysitron TI 950 Triboindenter at Frederick Seitz Materials Research Laboratory Central Facilities, University of Illinois. To demonstrate time dependent behavior of PMMA, indentation was carried out at two different loading rates. In the first experiment, 10 mN peak load was applied over 10 seconds. In the second experiment, a 10 mN force was applied over 100 seconds. For both experiments, a spherical tip (radius 93.64 μm) was used.

5.2.2. Viscoelastic simulation tool

Viscoelastic simulation tool on Nanohub can predict material parameters using experimental nanoindentation data. The tool uses Standard Linear Solid (SLS) model [6] for viscoelastic materials and fits experimental nanoindentation data numerically to compute material parameters.

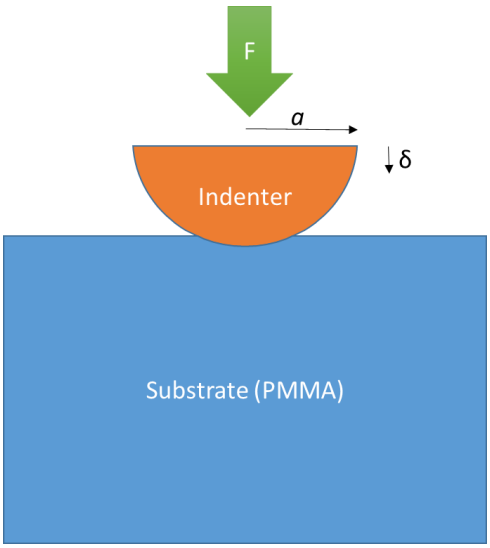

Figure 5.1: Schematic of nanoindentation

Figure 5.1 shows the schematic diagram of nanoindentation using spherical indenter. Solution for indentation of semi-infinite sample using a spherical indenter is given by –

$$F = \frac{4}{3} E^* a^{\frac{1}{2}} \delta^3 \qquad \text{Eq 5.1}$$

where F is applied force, a is the radius of indenter, δ is indentation depth and E^* is the reduced modulus for the substrate. Assuming a rigid indenter, reduced modulus is related to elastic modulus (E) and Poisson's ratio (ν) as

$$E^* = \frac{E}{1-\nu^2} = \frac{2G}{1-\nu} \qquad \text{Eq 5.2}$$

For this study, we have adopted a value of 0.375 for Poisson's ratio.

Eq. (5.1) can be rewritten as

$$\delta^{\frac{3}{2}} = \frac{3(1-\nu)}{4\sqrt{a}}\frac{F}{2G} \quad \text{Eq 5.3}$$

After replacing F/2G with corresponding viscoelastic term [2], we have the following equation

$$\delta(t)^{\frac{3}{2}} = \frac{3(1-\nu)}{4\sqrt{a}}\int_{-\infty}^{t} J(t-t')\frac{\mathrm{d}F(t')}{\mathrm{d}t'}\mathrm{d}t' \quad \text{Eq 5.4}$$

where $J(t)$ is the creep compliance function. Nanohub tool uses Standard Linear Solid models [6] in series, as shown in Figure 5.2.

Figure 5.2: SLS model

The creep compliance for *n* units of such a solid is given by

$$J(t) = B_0 + \sum_{1}^{n} B_i e^{-\frac{t}{T_i}} \quad \text{Eq 5.5}$$

where the constants B_0 and B_i are defined as

$$B_0 = \sum_{i=0}^{n} \frac{1}{G_i} \quad \text{Eq 5.6}$$

$$B_i = \frac{1}{G_i} \quad \text{Eq 5.7}$$

$$\tau_i = \frac{\eta_i}{G_i} \quad \text{Eq 5.8}$$

where G and η are corresponding spring and viscous constants.

For ramp loading, instantaneous force is given by

$$F(t) = \frac{F_{max}}{t_r}t \quad \text{Eq 5.9}$$

where t_r is the time for ramp load and F_{max} is the maximum force.

Substituting creep compliance function and force expression (5.5 and 5.6) in Eq. (5.4) and carrying out integration, we have

$$\delta(t)^{\frac{3}{2}} = \frac{3(1-\nu)F_{max}}{4t_r\sqrt{a}}\left(B_0 t - \sum_1^n B_i T_i\left(1 - e^{-\frac{t}{T_i}}\right)\right) \quad \text{Eq 5.10}$$

Eq. (5.10) is the generalized expression for indenter displacement during indentation of viscoelastic material. Viscoelastic simulation tool can simulate material for one or two SLS elements, yielding three or five material parameters respectively. In this study, we consider only 3 constants, hence Eq. (5.10) can be reduced as

$$\delta(t)^{\frac{3}{2}} = \frac{3(1-\nu)F_{max}}{4t_r\sqrt{a}}\left(B_0 t - B_1 T_1\left(1 - e^{-\frac{t}{T_1}}\right)\right) \quad \text{Eq 5.11}$$

5.3. Results

Load-displacement data as obtained from two different loading rates are shown in Figure 5.3.

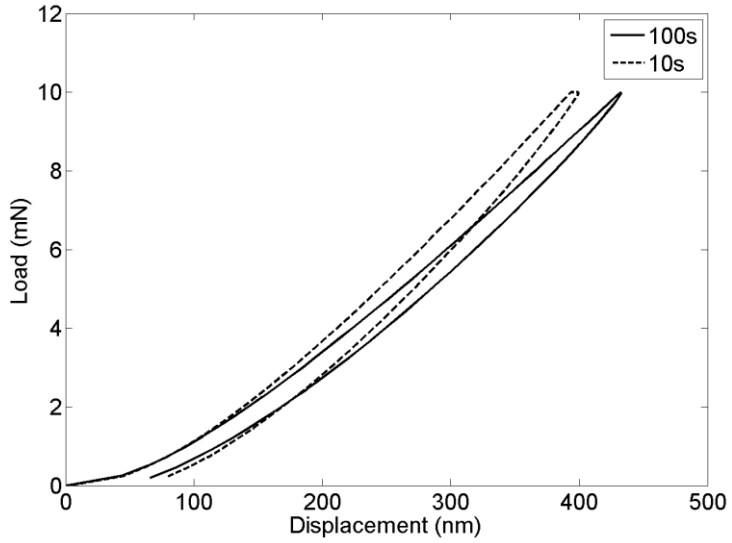

Figure 5.3: Experimental nanoindentation data for two different loading rates

It is evident from the plot that PMMA exhibits time dependent behavior. As expected, the indentation depth for faster loading ($t_r = 10s$) is smaller than for slower loading ($t_r = 100s$). Consequently, the unloading slopes are different for these two tests. Unloading slope for slower loading is 0.0361 N/m whereas unloading slope for faster loading is 0.0423N/m. Using Oliver and

Pharr formulation [58], we arrive at elastic modulus values of 2.27 GPa and 2.71 GPa, respectively. Clearly, faster loading results in an over-prediction of elastic modulus.

The Nanohub indentation tool yielded values listed in Table 5.1.

Table 5.1: Material parameters obtained from viscoelastic simulation tool

Parameter	Value
$\boldsymbol{B_0}$	$2.77\ x\ 10^{-8}\ Pa^{-1}$
$\boldsymbol{B_1}$	$2.72\ x\ 10^{-8}\ Pa^{-1}$
$\boldsymbol{\tau_1}$	$2.30\ x\ 10^{4}\ s$
$\boldsymbol{E_{initial}}$	$2.63\ x\ 10^{9}\ Pa$
$\boldsymbol{E_{\infty}}$	$4.97\ x\ 10^{7}\ Pa$

Figure 5.4 and 5.5 compares experimental and computational time-displacement data for 10 s loading and 100 s loading.

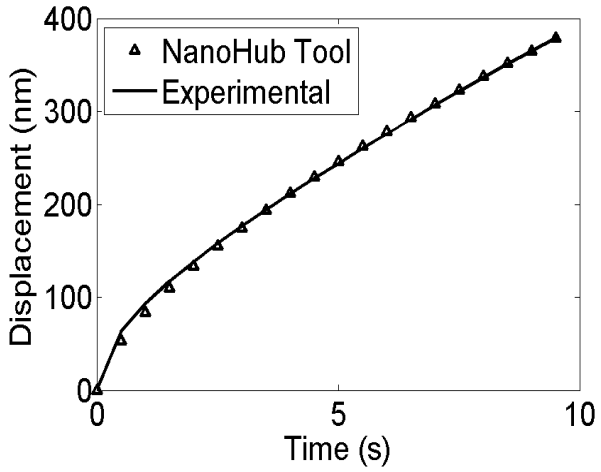

Figure 5.4: Time displacement data for 10 s loading time

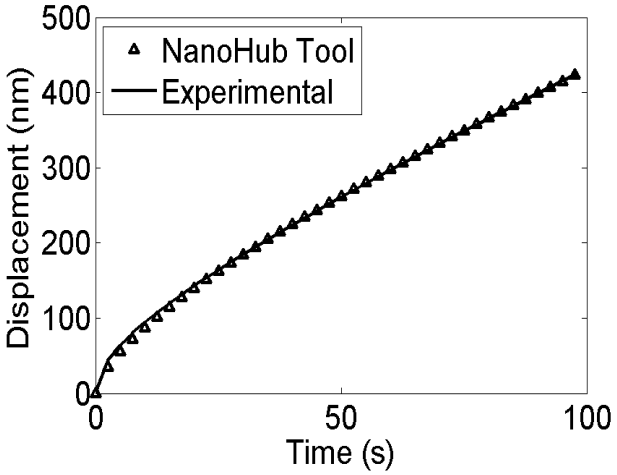

Figure 5.5: Time displacement data for 100 s loading time

From the plots, it can be seen that material parameters shown in Table 5.1 can predict the time displacement behavior for both experiments very precisely. The tool reports an elastic modulus value of 2.63 GPa.

5.4. Discussion

Viscoelastic simulation tool provides a fast and efficient way for characterizing viscoelastic parameters of soft materials. The tool, however, currently cannot provide any plastic or damage properties. Indentation using spherical indenters and low loads generally results in very low plastic deformations, hence viscoelastic material assumption is justified for this tool. In cases of large deformations (in case of sharp indenters) significant amount of plastic deformation and damage is observed and cannot be currently simulated using this tool.

REFERENCES

[1] Fischer-Cripps, A. C. (2011). *Nanoindentation*. Springer Science & Business Media.

[2] Lee, E. H., & Radok, J. R. M. (1960). The contact problem for viscoelastic bodies. *Journal of Applied Mechanics*, *27*(3), 438-444.

[3] Hansma, P. K., Turner, P. J., & Fantner, G. E. (2006). Bone diagnostic instrument. *Review of Scientific Instruments*, *77*(7), 075105.

[4] Frommeyer, G., & Rablbauer, R. (2008). High temperature materials based on the intermetallic compound NiAl reinforced by refractory metals for advanced energy conversion technologies.

[5] Goudarzi, T. (2015) Nanoindentation of soft viscoelastic materials, https://nanohub.org/resources/viscoindent. (DOI: 10.4231/D3GB1XJ0N).

[6] Oyen, M. L. (2006). Analytical techniques for indentation of viscoelastic materials. *Philosophical Magazine*, *86*(33-35), 5625-5641.

[7] Dietrich, C., Poech, M. H., Fischmeister, H. F., & Schmauder, S. (1993). Stress and strain partitioning in a Ag Ni fibre composite under transverse loading finite element modelling and experimental study. *Computational materials science*, *1*(3), 195-202.

[8] Wang, J., Hoagland, R. G., & Misra, A. (2009). Mechanics of nanoscale metallic multilayers: From atomic-scale to micro-scale. *Scripta Materialia*,*60*(12), 1067-1072.

[9] Dannemann, K., Stoloff, N. S., & Duquette, D. J. (1987). High temperature fatigue of three nickel-base eutectic composites. *Materials Science and Engineering*, *95*, 63-71.

[10] Needleman, A. (2000). Computational mechanics at the mesoscale. *Acta Materialia*, *48*(1), 105-124.

[11] Hutchinson, J. W., & Evans, A. G. (2000). Mechanics of materials: top-down approaches to fracture. *Acta materialia*, *48*(1), 125-135.

[12] Evans, A. G. (1998). Design and life prediction issues for high-temperature engineering ceramics and their composites. In *Ceramic Microstructures* (pp. 35-64). Springer US.

[13] Setters, A., & Jasiuk, I. (2014). Towards a standardized reference point indentation testing procedure. *Journal of the mechanical behavior of biomedical materials*, *34*, 57-65.

[14] Setters, A. (2014). *Investigation of age related changes in porcine cortical bone with a focus on the reference point indentation technique* (Master's thesis). University of Illinois, Urbana, IL.

[15] Li, Y., Zhang, Z., Vogt, R., Schoenung, J. M., & Lavernia, E. J. (2011). Boundaries and interfaces in ultrafine grain composites. *Acta Materialia*, *59*(19), 7206-7218.

[16] Beyerlein, I. J., Mara, N. A., Bhattacharyya, D., Alexander, D. J., & Necker, C. T. (2011). Texture evolution via combined slip and deformation twinning in rolled silver–copper cast eutectic nanocomposite. *International Journal of Plasticity*, *27*(1), 121-146.

[17] Yu, D., Bei, H., Chen, Y., George, E. P., & An, K. (2014). Phase-specific deformation behavior of a relatively tough NiAl–Cr (Mo) lamellar composite.*Scripta Materialia*, *84*, 59-62.

[18] Barabash, R. I., Liu, W., Tischler, J. Z., Bei, H., & Budai, J. D. (2012). Phase-specific elastic/plastic interface interactions in layered NiAl–Cr (Mo) structures.*Acta Materialia*, *60*(8), 3279-3286.

[19] Barabash, R. I., Bei, H., Gao, Y. F., & Ice, G. E. (2011). Interface strength in NiAl–Mo composites from 3-D X-ray microdiffraction. *Scripta Materialia*, *64*(9), 900-903.

[20] Frommeyer, G., Rablbauer, R., & Schäfer, H. J. (2010). Elastic properties of B2-ordered NiAl and NiAl–X (Cr, Mo, W) alloys. *Intermetallics*, *18*(3), 299-305.

[21] Bei, H., George, E. P., & Pharr, G. M. (2008). Small-scale mechanical behavior of intermetallics and their composites. *Materials Science and Engineering: A*,*483*, 218-222.

[22] Tartaglia, J. M., & Stoloff, N. S. (1981). Fatigue of Ni-Ai-Mo aligned eutectics at elevated temperatures. *Metallurgical Transactions A*, *12*(11), 1891-1898.

[23] Rablbauer, R., Frommeyer, G., & Stein, F. (2003). Determination of the constitution of the quasi–binary eutectic NiAl–Re system by DTA and microstructural investigations. *Materials Science and Engineering: A*, *343*(1), 301-307.

[24] Guo, J. T., Huai, K. W., Gao, Q., Ren, W. L., & Li, G. S. (2007). Effects of rare earth elements on the microstructure and mechanical properties of NiAl-based eutectic alloy. *Intermetallics*, *15*(5), 727-733.

[25] Tang, L. Z., Zhang, Z. G., Li, S. S., & Gong, S. K. (2010). Mechanical behaviors of NiAl-Cr (Mo)-based near eutectic alloy with Ti, Hf, Nb and W additions. *Transactions of Nonferrous Metals Society of China*, *20*(2), 212-216.

[26] Sheng, L. Y., Zhang, W., Guo, J. T., Zhou, L. Z., & Ye, H. Q. (2009). Microstructure evolution and mechanical properties' improvement of NiAl–Cr (Mo)–Hf eutectic alloy during suction casting and subsequent HIP treatment.*Intermetallics*, *17*(12), 1115-1119.

[27] Sheng, L. Y., Xie, Y., Xi, T. F., Guo, J. T., Zheng, Y. F., & Ye, H. Q. (2011). Microstructure characteristics and compressive properties of NiAl-based multiphase alloy during heat treatments. *Materials Science and Engineering: A*,*528*(29), 8324-8331.

[28] Huai, K. W., Guo, J. T., Ren, Z. R., Gao, Q., & Yang, R. (2006). Effect of nb on the microstructure and mechanical properties of cast NiAl-Cr (Mo) eutectic alloy.

[29] Yang, J. M., Jeng, S. M., Bain, K., & Amato, R. A. (1997). Microstructure and mechanical behavior of in-situ directional solidified NiAl/Cr (Mo) eutectic composite. *Acta materialia*, *45*(1), 295-308.

[30] Barabash, R., & Ice, G. E. (2014). *Strain and dislocation gradients from diffraction*. Oak Ridge National Laboratory (ORNL).

[31] Barabash, R., Ice, G. E., Larson, B. C., Pharr, G. M., Chung, K. S., & Yang, W. (2001). White microbeam diffraction from distorted crystals. *Applied Physics Letters*, *79*(6), 749-751.

[32] Yang, W., Larson, B. C., Ice, G. E., Tischler, J. Z., Budai, J. D., Chung, K. S., & Lowe, W. P. (2003). Spatially resolved Poisson strain and anticlastic curvature measurements in Si under large deflection bending. *Applied physics letters*, *82*(22), 3856-3858.

[33] Ice, G. E., Budai, J. D., & Pang, J. W. (2011). The race to x-ray microbeam and nanobeam science. *Science*, *334*(6060), 1234-1239.

[34] Wang, L., Barabash, R., Bieler, T., Liu, W., & Eisenlohr, P. (2013). Study of\{11\ bar {2} 1\} Twinning in α-Ti by EBSD and Laue Microdiffraction. *Metallurgical and Materials Transactions A*, *44*(8), 3664-3674.

[35] Barabash, R. I., Barabash, O. M., Ojima, M., Yu, Z., Inoue, J., Nambu, S., & Feng, Z. (2014). Interphase strain gradients in multilayered steel composite from microdiffraction. *Metallurgical and Materials Transactions A*, *45*(1), 98-108.

[36] Abaqus, (2013) *Abaqus / Standard Analysis User's Manual*, version 6.13.

[37] Koric, S., & Thomas, B. G. (2006). Efficient thermo-mechanical model for solidification processes. *International journal for numerical methods in engineering*, *66*(12), 1955-1989.

[38] Zienkiewicz, O. C., & Taylor, R. L. (2005). *The finite element method for solid and structural mechanics*. Butterworth-Heinemann.

[39] Koric, S., Lu, Q., & Guleryuz, E. (2014). Evaluation of massively parallel linear sparse solvers on unstructured finite element meshes. *Computers & Structures*, *141*, 19-25.

[40] Fish, J., & Belytschko, T. (2007). *A first course in finite elements*. John Wiley & Sons.

[41] iForge. iForge-NCSA's Exclusive Industrial HPC resource. 2013; Available from: <http://www.ncsa.illinois.edu/News/12/0709NCSAiForge.html>.

[42] Ding, Y. Y., Adschiri, T., Williams, G. A., Callon, K. E., Watson, M., Naot, D., ... & Cornish, J. (2011). Validation of BioDent TDI as a New Clinical Diagnostic Method. *Advanced Materials Research*, *275*, 151-154.

[43] Zhang, J., Michalenko, M. M., Kuhl, E., & Ovaert, T. C. (2010). Characterization of indentation response and stiffness reduction of bone using a continuum damage model. *Journal of the mechanical behavior of biomedical materials*, *3*(2), 189-202.

[44] Carter, D. R., & Hayes, W. C. (1976). Bone compressive strength: the influence of density and strain rate. *Science*, *194*(4270), 1174-1176.

[45] Jämsä, T., Jalovaara, P., Peng, Z., Väänänen, H. K., & Tuukkanen, J. (1998). Comparison of three-point bending test and peripheral quantitative computed tomography analysis in the evaluation of the strength of mouse femur and tibia.*Bone*, *23*(2), 155-161.

[46] Norman, T. L., Vashishth, D., & Burr, D. B. (1995). Fracture toughness of human bone under tension. *Journal of biomechanics*, *28*(3), 309-320.

[47] Gallant, M. A., Brown, D. M., Organ, J. M., Allen, M. R., & Burr, D. B. (2013). Reference-point indentation correlates with bone toughness assessed using whole-bone traditional mechanical testing. *Bone*, *53*(1), 301-305.

[48] Rasoulian, R., Najafi, A. R., Chittenden, M., & Jasiuk, I. (2013). Reference point indentation study of age-related changes in porcine femoral cortical bone.*Journal of biomechanics*, *46*(10), 1689-1696.

[49] Aref, M., Gallant, M. A., Organ, J. M., Wallace, J. M., Newman, C. L., Burr, D. B., ... & Allen, M. R. (2013). In vivo reference point indentation reveals positive effects of raloxifene on mechanical properties following 6months of treatment in skeletally mature beagle dogs. *Bone*, *56*(2), 449-453.

[50] Mellibovsky, L., Prieto-Alhambra, D., Mellibovsky, F., Güerri-Fernández, R., Nogués, X., Randall, C., & Díez-Perez, A. (2015). Bone Tissue Properties Measurement by Reference Point Indentation in Glucocorticoid-Induced Osteoporosis. *Journal of Bone and Mineral Research*.

[51] Bhattacharya, A. K., & Nix, W. D. (1988). Finite element simulation of indentation experiments. *International Journal of Solids and Structures*, *24*(9), 881-891.

[52] Knapp, J. A., Follstaedt, D. M., Myers, S. M., Barbour, J. C., & Friedmann, T. A. (1999). Finite-element modeling of nanoindentation. *Journal of Applied Physics*, *85*(3), 1460-1474.

[53] Komvopoulos, K. (1989). Elastic-plastic finite element analysis of indented layered media. *Journal of Tribology*, *111*(3), 430-439.

[54] Zhang, J., Niebur, G. L., & Ovaert, T. C. (2008). Mechanical property determination of bone through nano-and micro-indentation testing and finite element simulation. *Journal of biomechanics*, *41*(2), 267-275.

[55] Lubliner, J., Oliver, J., Oller, S., & Onate, E. (1989). A plastic-damage model for concrete. *International Journal of solids and structures*, *25*(3), 299-326.

[56] Phipps, S., Yang, T. H. J., Habib, F. K., Reuben, R. L., & McNeill, S. A. (2005). Measurement of tissue mechanical characteristics to distinguish between benign and malignant prostatic disease. *Urology*, *66*(2), 447-450.

[57] Ebihara, T., Venkatesan, N., Tanaka, R., & Ludwig, M. S. (2000). Changes in Extracellular Matrix and Tissue Viscoelasticity in Bleomycin–induced Lung Fibrosis: Temporal Aspects. *American journal of respiratory and critical care medicine*, *162*(4), 1569-1576.

[58] Oliver, W. C., & Pharr, G. M. (1992). An improved technique for determining hardness and elastic modulus using load and displacement sensing indentation experiments. *Journal of materials research*, *7*(06), 1